

Section 4

Parameterization of important atmospheric and surface processes, effects of different parameterizations

Analysis of the Numerics of Physics-Dynamics Couplingⁱ

Mark Dubal, Nigel Wood and Andrew Staniforth, Met Office, UK.

mark.dubal@metoffice.gov.uk

Physics parametrization packages are key elements in the success of numerical weather and climate prediction models. The accuracy and complexity of these schemes continues to increase apace. Similarly, the accuracy of dynamical cores has continued to steadily improve. However, a chain is only as strong as its weakest link, e.g. two 2nd-order components coupled in a 1st-order manner imply a 1st-order model. The link coupling the physics package to the inviscid, adiabatic dynamical core has received little attention. It is therefore important for the continued improvement of models that the virtues and vices of the various strategies employed in such coupling are well understood, and that the vices are addressed.

However, in a model there are several distinct processes (e.g. the dynamical core and each component of the physics package) each with their own timescale(s). The use of an implicit scheme to solve simultaneously for the time tendency of the complete model, though appealing, is currently prohibitively expensive, at least in an operational setting, and is likely to remain so for the foreseeable future. This is because of the expense of solving a modified Helmholtz problem which consists of contributions from both the dynamics *and* the physics package. The solution is to apply some form of splitting in which the time tendency due to the different elements of a model are evaluated separately, and then combined in some way to generate the complete model tendency. All operational models employ some form of splitting. The problem is that splitting in general introduces errors additional to the truncation errors associated with each individual process. With large timesteps, of the size permitted by semi-implicit semi-Lagrangian schemes, such errors can dominate the model error. The question is therefore: “How to determine the optimal way of performing such splitting?”

A methodology for analyzing the numerical properties of such splitting schemes is developed in Staniforth et al. (2002*a*) and Staniforth et al. (2002*b*). A canonical problem is introduced to idealize both the dynamics (with terms to represent both fast and slow propagating modes), and the parametrizations of fast and slow, oscillatory and damped, physical processes. It permits the examination of a broad set of physics-dynamics coupling issues, whilst keeping the analysis tractable. Any given coupling scheme can be assessed in terms of its numerical stability and of the accuracy of both its transient and steady-state responses.

For the reasons discussed above, fully implicit coupling is impracticable, as is fully explicit coupling due to timestep restrictions. A popular approach is “split-implicit” coupling in which a dynamics predictor is followed by a physics corrector. It addresses the stability issue of an explicit coupling whilst keeping the physics discretization distinct from the dynamics discretization. However, using the framework of Staniforth et al. (2002*a*) and Staniforth et al. (2002*b*), it is found that the steady-state solution is corrupted and the forced response can be spuriously amplified by an order-of-magnitude. This motivated the “symmetrized split-implicit” coupling in which two physics discretizations are arranged symmetrically around a dynamics sub-step. The analysis shows that this addresses the stability and accuracy deficiencies of an explicit coupling whilst still correctly representing the exact steady-state solution for constant forcing. It also keeps the physics discretization distinct from the dynamics one. It partially shares the disadvantage of the fully implicit model inasmuch as the second physics sub-step is an implicit discretization of the highly nonlinear physics. However the usual column-based

ⁱ© British Crown Copyright

physical parametrizations are such that the discrete set of nonlinear equations can be solved column-by-column, greatly reducing the computational cost.

This early work was done in the context of a physics package comprising only one component. In a typical model, however, there are at least four distinct components, each with different characteristics. The work of Dubal et al. (2004) and Dubal et al. (2005) therefore extends the above-described framework to examine the coupling of a mix of physical parametrizations of various damping and oscillatory processes associated with a range of timescales. Various coupling strategies have been examined but none has been found which performs uniformly well. Only rather general conclusions can be drawn. For example, there are two generic splitting schemes: sequential-splitting, in which the model's tendency is updated sequentially using the tendency due to each physics component in turn; and parallel-splitting, in which the model's tendency is updated simply by summing, independently, the tendencies of each physics component. It is found that sequential splitting is more flexible in its ability to eliminate splitting errors than parallel splitting. A disadvantage is that the sequential approach is sensitive to the order in which the physics components are applied. In practice a mix of sequential schemes for the fast timescale physics, and parallel schemes for the slow timescale ones, appears to optimize the overall coupling strategy. It is then found that the slower processes, such as radiation, should appear near the centre of the timestep, with the faster processes, such as boundary layer diffusion, coupled implicitly at the end of the timestep.

The framework of Staniforth et al. (2002a) and Staniforth et al. (2002b) can also be used to analyze the problem of spurious computational resonance in a semi-implicit semi-Lagrangian model. Traditionally, this has arisen in the presence of stationary spatial forcing, specifically that due to orography (Rivest et al. 1994). In this case, spurious resonance is absent when a Courant number restriction on timestep is satisfied. Staniforth et al. (2002a) show that time-dependent forcing, such as that due to the physics package, can also give rise to spurious resonance. Importantly though, the Courant number limitation on the timestep is then twice as restrictive as that for stationary forcing, thereby exacerbating the problem of spurious computational resonance with long timesteps.

References

- Dubal, M., Wood, N. & Staniforth, A. 2004 , Analysis of parallel versus sequential splittings for time-stepping physical parameterizations, *Mon. Wea. Rev.* **132**, 121–132.
- Dubal, M., Wood, N. & Staniforth, A. 2005 , Mixed parallel-sequential split schemes for time-stepping multiple physical parameterisations, *Mon. Wea. Rev.* (to appear).
- Rivest, C., Staniforth, A. & Robert, A. 1994 , Spurious resonant response of semi-Lagrangian discretisations to orographic forcing: diagnosis and solution, *Mon. Wea. Rev.* **122**, 366–376.
- Staniforth, A., Wood, N. & Côté, J. 2002a , Analysis of the numerics of physics-dynamics coupling, *Q. J. R. Meteorol. Soc.* **128**, 2779–2799.
- Staniforth, A., Wood, N. & Côté, J. 2002b , A simple comparison of four physics-dynamics coupling schemes, *Mon. Wea. Rev.* **130**, 3129–3135.

WRF Modelling System Experiments With Different Land-Surface Options

Juan Ferreira*, Carlos Marques, Alfredo Rocha and Paulo Gonçalves
Department of Physics, Campus de Santiago, University of Aveiro, 3810-193 Aveiro,
Portugal
*juan@fis.ua.pt

1. Introduction

In this study, we present some results of the Weather Research and Forecast (WRF) modelling system with different land-surface schemes. These results are from a WRF 48 hours forecast in the autumn season (22th and 23th November 2004). The purpose of the study is to evaluate the effects of the different land-surface models available in the WRF modelling system on the predicted 2-meter temperature over Portugal.

2. Experiments

For these experiments we had used a single domain with 30 km horizontal resolution centred at the Iberian Peninsula. This domain uses 26 vertical levels, with the model top at 50 mb. The model is initialised with 1° resolution AVN datasets. For the initialisation of soil conditions it was used the global geographical information tiles for the WRF Standard Initialisation (WRFSI) system. We performed three simulations for the same location and for the same period of time, only varying the land-surface schemes: the thermal diffusion scheme (Dudhia, 1996), the Noah land surface model (Ek et al, 2003) and the RUC model (Smirnova, 2000). These three models were used with the following non-soil physics options: i) the Mellor-Yamada-Janjic PBL scheme, ii) the Kain-Fritsch cumulus parameterisation scheme, iii) the Monin-Obukhov-Janjic surface-layer parameterisation scheme and iv) the Dudhia radiation scheme.

3. Results and Conclusions

The results of the experiments were compared with 6 stations distributed along Portugal. In general, with respect to the 2-meter temperature, we observed that the Thermal and RUC models have quite similar behaviours, while the Noah land-surface model tends to predict higher 2-meter temperature values, as can be seen, for example, in Coimbra (Fig. 1). However, in most of the stations compared, the Thermal and RUC schemes tend to underestimate the maximum temperature whilst the Noah land-surface model predictions of the maximum 2-meter temperature are more accurate. The minimum temperature was badly predicted in all experiments.

Manifestly, the predicted temperature evolution shows insufficient accuracy in these three experiments, especially for the minimum temperature. This indicates that, in order to

obtain better temperature predictions, the land-surface schemes have to be combined with other non-soil physics options. One example we obtained that clearly improves the 2-meter temperature predictions, combines the thermal diffusion scheme with the Monin-Obukhov surface-layer parameterisation scheme and the YSU PBL scheme.

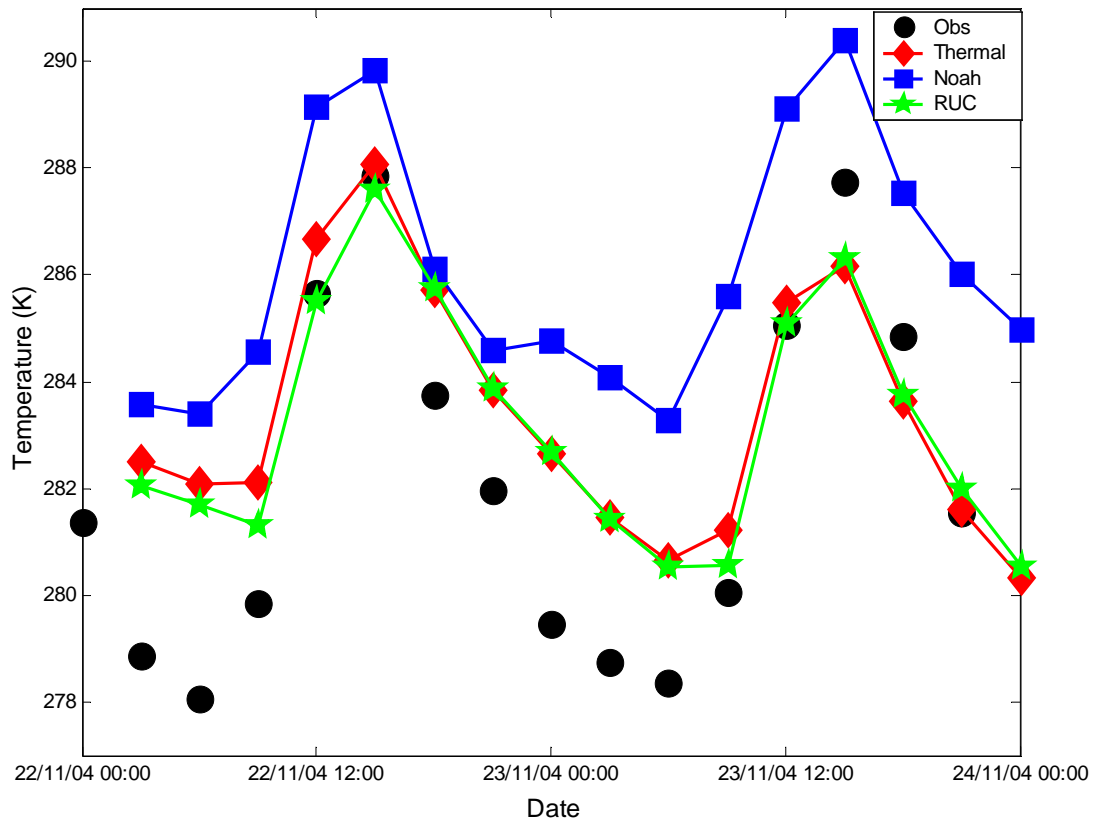


Figure 1 – 2-meter temperature evolution for Coimbra. Observed data (circles), RUC scheme (stars), thermal scheme (diamonds) and Noah land-surface model (squares).

References

Dudhia, J., 1996: A multi-layer soil temperature model for MM5. Preprints, 6th Annual MM5 Users Workshop, Boulder, CO.

Ek, M.B., K. E. Mitchell, Y. Lin, E. Rogers, P. Grummann, V. Koren, G. Gayno and J. D. Tarpley, 2003: Implementation of Noah land-surface model advances in the NCEP operational mesoscale Eta mode. *J. Geophys. Res.*, 108 (D22): No. 8851 NOV 29.

Smirnova, T. G., J. M. Brown, S. G. Benjamin, and D. Kim, 2000: Parameterization of cold-season processes in the MAPS land-surface scheme. *J. Geophys. Res.*, 105 (D3): No. 4077-4086 Feb 16.

Implementation of a 3D-Turbulence Parameterization for the Very Short Range Forecast Model LMK

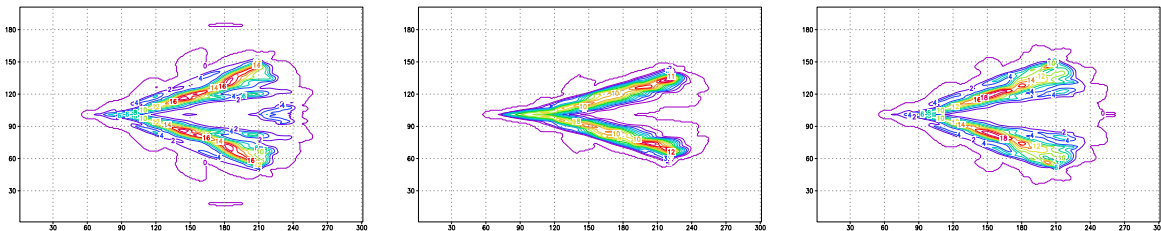
Jochen Förstner, Hans-Joachim Herzog, Gerd Vogel
 Deutscher Wetterdienst, Kaiserleistr. 35, 63067 Offenbach am Main
 E-mail: jochen.foerstner@dwd.de, hans-joachim.herzog@dwd.de, gerd.vogel@dwd.de

The model LMK ('LM Kürzestfrist') which aims at very short range weather forecasts in the meso- γ -scale (about 2.5-3 km) is currently developed at the Deutscher Wetterdienst (DWD) (Doms and Förstner 2004; Baldauf et al. 2005). This development includes the introduction of a new dynamical core (Förstner and Doms 2004) and new physical parameterizations for cloud microphysics (Reinhardt 2005) and 3-dimensional turbulence into the framework of the LM (Doms and Schättler 2002). In the operational 7 km version of the LM only vertical diffusion is taken into account, but as we go to higher and higher resolutions the inclusion of horizontal diffusion will become relevant. If this is already the case at a spatial resolution about 3 km is still open for discussion.

The 3D-turbulence scheme was originally developed for the LITFASS project of the DWD (Herzog et al. 2002) with a Smagorinski-type scheme and was used for LES simulations. To be applicable at the planned resolution of the LMK a Mellor-Yamada-type parameterization was added. Implementation of this scheme for LMK mainly consisted in the adaption to the new 2-timelevel Runge-Kutta core. In particular the inclusion of the horizontal diffusion terms for momentum, heat and moisture, as well as the integration of the prognostic TKE equation. Up to now several metric terms related to the coordinate transformations are neglected in the formulation of the horizontal terms and it will be further investigated if this approximation is justified. The advection and diffusion of TKE is solved in a way equivalent to the other scalar prognostic quantities. We use the following parameterized version of the TKE equation:

$$\begin{aligned} \frac{\partial \bar{e}}{\partial t} + \bar{u}_j \frac{\partial \bar{e}}{\partial x_j} = & 2 \left(\frac{\partial}{\partial x_1} \left(K_m^H \frac{\partial \bar{e}}{\partial x_1} \right) + \frac{\partial}{\partial x_2} \left(K_m^H \frac{\partial \bar{e}}{\partial x_2} \right) + \frac{\partial}{\partial x_3} \left(K_m^V \frac{\partial \bar{e}}{\partial x_3} \right) \right) \\ & + K_m^H S_H^2 + K_m^V S_V^2 - K_h^V N^2 - c_\epsilon \frac{\bar{e}^{\frac{3}{2}}}{l}. \end{aligned} \quad (1)$$

Here we introduce a distinction between K^H and K^V where the horizontal diffusion coefficients are determined from the vertical ones by use of an anisotropy factor proportional to the aspect ratio of the mesh. This is done for the sake of simplicity and will be replaced by more sophisticated methods in the near future. Compared to the operational parameterization of the LM (Raschendorfer 2001) the one used in the 3D scheme misses a number of features. Most important only a preliminary treatment of moist turbulence is included where for example only grid scale cloudiness is taken into account. Also missing is a parameterization for subscale thermal circulations. Therefore it is planned to combine the straightforward implementation of the horizontal diffusion terms and integration of the TKE in the new dynamical core described above with the more sophisticated parameterizations of the operational scheme in the beginning of 2005.



(a) New 3D-turbulence parameterization – moist (*only preliminary consideration of grid scale clouds*).

(b) Operational 1D-turbulence parameterization – moist (*consideration of grid scale clouds*).

(c) Operational 1D-turbulence parameterization – dry (*no consideration of clouds*).

Figure 1: Accumulated Precipitation in colored contour lines. Results of LMK simulations with TVD-RK-3rd / UP-5th dynamics after a simulation time of 192 min – $\Delta t = 6$ s; $\Delta x, \Delta y = 1$ km.

An idealized study reveals the relevance of the advanced moist turbulence formulation in the operational scheme. Figure 1 shows the accumulated precipitation for a storm splitting test case (Weisman and Klemp 1982) with $U_{max} = 25$ m/s and $q_{max} = 14$ g/kg.

In spite of the restrictions mentioned, the new scheme runs stable and produces realistic results. As an example Figure 2 shows a comparison of a precipitation forecast using the two different schemes. At least in this real case study the two schemes produce very similar results with only a bit less precipitation when the new 3D scheme is used.

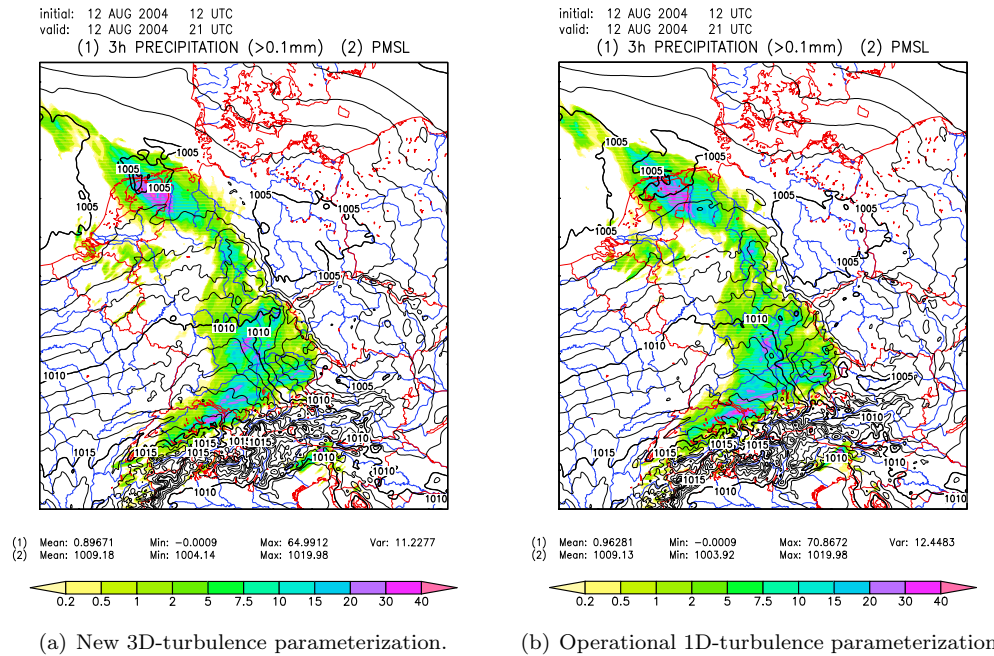


Figure 2: Forecast for 12 August 2004, 21 UTC. Shown in shaded colors is the 3 h accumulated precipitation and the pressure at mean sea level in black contour lines. Results of LMK simulations with TVD-RK-3rd / UP-5th dynamics after a simulation time of 9 h - $\Delta t = 30$ s; $\Delta x, \Delta y = 2.8$ km.

References

- Baldauf, M., J. Förstner, and P. Prohl, 2005: Idealized Tests of the Very Short-Range Forecast Model LMK. *WGNE Blue Book*, <http://www.cmc.ec.gc.ca/rpn/wgne/>
- Doms, G., and U. Schättler, 2002: A Description of the Nonhydrostatic Regional Model LM. <http://cosmo-model.cscs.ch/cosmoPublic/>
- Doms, G., and J. Förstner, 2004: Development of a NWP System for Very Short-Range Forecasts. *WGNE Blue Book*, <http://www.cmc.ec.gc.ca/rpn/wgne/>
- Förstner, J., and G. Doms, 2004: Runge-Kutta Time Integration and High-Order Spatial Discretization — a New Dynamical Core for the LMK. *WGNE Blue Book*, <http://www.cmc.ec.gc.ca/rpn/wgne/>
- Herzog, H.-J., U. Schubert, G. Vogel, A. Fiedler, and R. Kirchner, 2002: LLM — the High-Resolving Nonhydrostatic Simulation Model in the DWD-Project LITFASS Part I: Modelling Technique and Simulation Method. *COSMO Technical Report*, No. 4, <http://cosmo-model.cscs.ch/cosmoPublic/>
- Raschendorfer, M., 2001: The New Turbulence Parameterization of LM. *COSMO Newsletter*, No. 1, 89–97, <http://cosmo-model.cscs.ch/cosmoPublic/>
- Reinhardt, T., 2005: A Prognostic Graupel Microphysics Scheme for High-Resolution NWP. *WGNE Blue Book*, <http://www.cmc.ec.gc.ca/rpn/wgne/>
- Weisman, M. L., and J. B. Klemp, 1982: The Dependence of Numerically Simulated Convective Storms on Vertical Wind Shear and Buoyancy. *Mon. Wea. Rev.*, 110, 504–520.

A new 'bracketing' technique for a flexible and economical computation of thermal radiative fluxes, scattering effects included, on the basis the Net Exchanged Rate (NER) formalism.

Jean- François Geleyn, Czech Hydrometeorological Institute, Prague, Czech Republic (*)
Richard Fournier, Laboratoire d'Energétique, Université Paul Sabatier, Toulouse, France
Gwenaëlle Hello, Centre National de Recherches Météorologiques, Météo- France, Toulouse
Neva Pristov, Environmental Agency of Slovenia, Ljubljana, Slovenia
(*) on leave of absence from Meteo- France

email: Jean- Francois.Geleyn@chmi.cz

The Net Exchanged Rate (NER) formalism (Green, 1967) offers several theoretical advantages with respect to other competing methods for thermal radiative computations: simplicity, since it allows to neglect the paths of all photons symmetrically exchanged between two atmospheric layers or between the surface and one of them, the interest being focussed only on those photons without counterpart; realism, since the warmer part of the exchange always loses energy to the colder one, whatever approximations may be used for computing transmissivities; accuracy, since it ensures energy conservation principles for the whole atmospheric column taken together with its underlying surface.

But, from a more practical point of view, NER allows stratifying the $N(N+1)/2$ thermal exchange terms between primary and secondary ones, N being the number of discretised layers along the vertical. Experience shows (Eymet et al., 2005) that, in the absence of cloud screening, the primary terms are threefold: cooling to space (CTS), exchange with surface (EWS) and exchange with the adjacent layers (EAL).

In this study we are treating the scattering effects (and in fact all cloudy effects) for these primary terms through a technique already introduced in 1992 in the operational models of Meteo- France: the gaseous optical thicknesses under which any given layer is seen from (A, the top of the atmosphere - CTS-, B, the surface -EWS- and C, either of its edges) are first computed as exactly as possible in a gas- only idealised atmosphere. These computations are of the band- model type. The obtained optical thicknesses are then injected back locally in two- stream + adding computations including all non- gaseous effects. One can readily show that this allows treating with an excellent accuracy the long- wave radiative interaction between multiple scattering and the very high spectral dependency of gaseous absorption rates, for those three cases (CTS, EWS and EAL) where the source/sink of the photons exchanged with the considered layer is unambiguously known. In these particular cases, there is in fact an analogy with the solar radiative computations, especially for the CTS case, where the thermal photons are following a kind of return path with respect to the solar ones (see for instance Ritter and Geleyn, 1992).

But this treatment leaves aside the majority of the exchange terms, which, although smaller than the primary ones, cannot be neglected. If one would like to reach the same relative accuracy than for the primary ones, it would be necessary to do a full 'emissivity- like' computation of all paired optical thicknesses and to then solve the two- stream & adding system $N+1$ times rather than something like 4 times. Needless to say, this destroys all the economy advantages of NER and of our advocated technique for the inclusion of scattering effects. Coming back to the above- mentioned stratification of the NER terms, we are however seeking absolute accuracy rather than relative accuracy and we may thus admit a more approximate treatment of these additional terms.

The method advocated here for this purpose relies on a simple fact. When knowing the CTS, EWS and EAL gaseous- only optical thicknesses relative to one given layer, **we already have the minimum and maximum optical thicknesses under which this layer is seen from any part of the gas- only atmosphere.** Indeed the former is the minimum of the CTS and EWS values and the latter is the EAL value. Hence, without any additional expensive computation of gaseous transmissions functions and with only a doubling of the number of two- stream + adding solvers, we are able to bracket the truth between computations with maximum and minimum estimated optical thicknesses for the terms other than CTS, EWS and EAL.

This way of dealing with the 'multiple source - multiple sinks' core problem of thermal radiative transfer shifts the problem to the search of an adequate set of interpolation coefficients for retrieving the best possible estimate of the truth, starting from its two 'bracketing values'. We first verified that the accuracy of such an interpolation is far better when applying it to the fluxes rather than to the cooling rates (both methods were a priori possible).

Arrived at this point, two strategies are possible:

To aim at an intermittent type of expensive radiative computations: the above-mentioned full pairing of layers is done from time to time, together with the max and min calculations, the interpolation weights are inferred and kept constant over several model time steps while recomputing only the cheap part of the procedure. This has not yet been tried but is one of our next goals to do it.

To search for a statistical parameterisation of the local values of the weighting coefficient α between min (0) and max (1). Stratifying a big amount of data, we found that α increases when the local gas absorption potential increases, i.e. lower down in the atmosphere as well as when there are strong changes of the basic vertical temperature gradient, i.e. in inversions. These are of course two expected behaviours since high alpha values means taking relatively more into account the local exchanges of photons.

Encouraged by the apparently wide validity of these findings we tried the following purely heuristic parameterisation:

$$\alpha = 0.3(p/p_s) + 0.1C_p(\partial\theta/\partial\Phi)$$

Even with this very simple fitting, results show a lot of improvements of the new parameterisation with respect to its old counterpart (where EAL was treated as a secondary process and α was consequently implicitly set to zero). Except for small problems in the stratosphere, the statistical fit with only two tuning constants works very well (see below the dispersion diagram of fluxes between their exact and retrieved values in one example). In the ARPEGE NWP model of Meteo-France, use of the new parameterisation leads to scores equal or slightly better than those of the old version of the ECWMF scheme with still a tenfold reduction in cost when both are compared in stand-alone mode for models with about forty levels. The scheme is already operational at CHMI and in the ALADIN contribution to the Europroject MFSTEP. Our goal is now to fit as closely as possible the RRTM transmission functions with the needed band-model-type calculation, in order to see which better cost-accuracy balance might be achieved with the 'statistical' version of the new scheme, before attacking the intermittency issue.

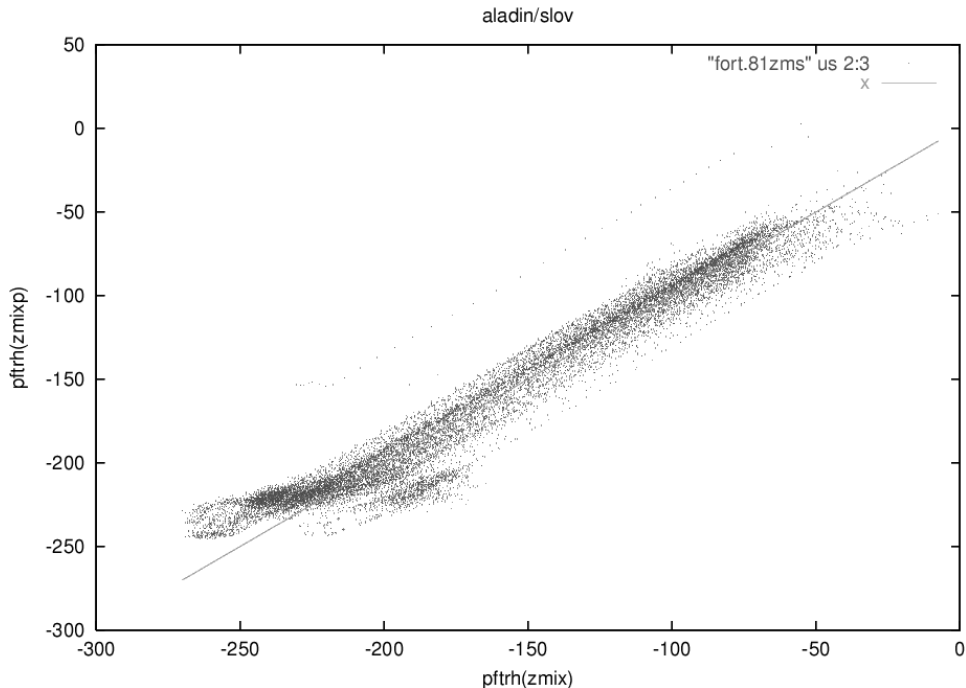


Figure: Dispersion diagram of thermal fluxes. X-axis: exact values. Y-axis : retrieved values from the parametrization.

Eymet, V. , J.-L. Dufresne, R. Ricchiazzi, R. Fournier and S. Blanco, 2005, to appear in Atmospheric Research.

Green, J.S.A., 1967, Quart. J. Roy. Met. Soc., 93, pp. 371- 372

Ritter, B. and J.-F. Geleyn, 1992, Mon. Wea. Rev., 120, pp. 303- 325.

The Enhancement of Condensation in Melting Layer Simulated by Cloud Resolving Non-hydrostatic Model

Akihiro HASHIMOTO¹, Masataka MURAKAMI², Chiashi MUROI², Sachie KANADA¹, Yasutaka WAKAZUKI¹, Kazuaki YASUNAGA¹, Teruyuki KATO², Kazuo KURIHARA², Masanori YOSHIZAKI²

¹Advanced Earth Science and Technology Organization, Tokyo

²Meteorological Research Institute / Japan Meteorological Agency, Tsukuba

1. Introduction

In order to examine the change of precipitation intensity around Japan under the situation of global warming and to contribute IPCC, we have conducted numerical simulations with the regional climate model with 5-km horizontal resolution which has been developed on the basis of JMA-NHM (Japan Meteorological Agency Non-Hydrostatic Model; Saito et al., 2001). In those numerical simulations, the condensation growth of cloud droplets was found to be enhanced in melting layer so that the heating by condensation exceeded the cooling due to the melting of snow particles in the layer. We are investigating how this enhancement of condensation occurred in the numerical experiments in order to ascertain whether this phenomenon can be realized in nature or not. A sensitivity test was done for this purpose and its result is reported here.

2. Numerical experiments

The microphysical processes in JMA-NHM are formulated with a bulk parameterization composed of three solid (ice, snow, graupel) and two liquid (cloud, rain) water categories. All of the categories are represented by a two-moment parameterization which has two prognostic variables, mixing ratio and number concentration in each category. The condensation growth of cloud droplets is formulated with saturation adjustment method. For the melting rate of snow and graupel particles, the heat budget relevant to melting and evaporation is considered.

When we conducted the simulations to contribute to IPCC, the model domain was set to cover the area of 4000x3000 km² over East Asia with 5-km horizontal resolution. However, we set the smaller domain with the area of 1500x1500 km² centered at west Japan shown in Fig. 1 to save a computational resource, when we conduct a sensitivity test in order to investigate the processes which cause the enhancement of condensation in melting layer. Vertically, 48 layers with variable intervals of 40 m to 960 m were employed. The model top is located at about 22 km. Integrated time interval is 12 s. The integration is conducted up to 24 hours. We referred the result of the global warming simulation with global climate model along the IPCC's A1B scenario as the

*Corresponding author address: Akihiro Hashimoto, Meteorological Research Institute, 1-1 Nagamine, Tsukuba, Ibaraki 305-0052 Japan; e-mail: ahashimo@mri-jma.go.jp

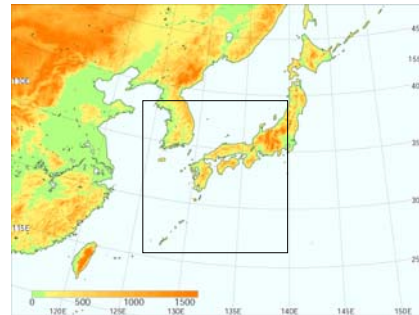


Fig. 1 The simulation domain with the area of 4000x3000 km² for the IPCC contribution. The inside rectangle corresponds to the domain with the area of 1500x1500 km² adopted in the sensitivity test.

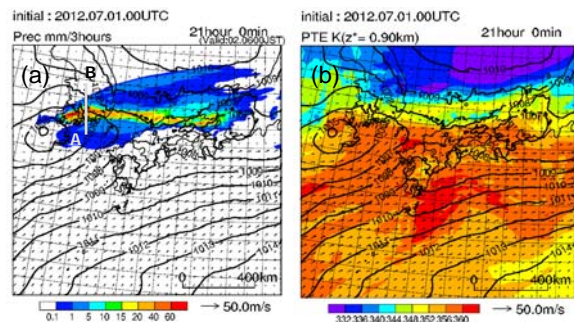


Fig. 2 (a) Precipitation (color) and wind (vector) at the surface. (b) Equivalent potential temperature (color) and wind (vector) at 900 m. Contour indicates sea level pressure. initial and boundary conditions. For the sensitivity test, we conducted two simulations; one considered the cooling resulted by melting of snow and graupel particles (EXP1) and another neglected (EXP2).

3. Simulation results

Figure 2a shows the precipitation distribution for the particular case simulated under the global warming situation. An intense precipitation band extends from Korean peninsula to the coast of west Japan. The difference of equivalent potential temperature θ_e is more than 20 K for 200-km distance crossing the precipitation band (Fig. 2b), which indicates that the air with high θ_e from south comes upon the air with low θ_e and is lifted so as to generate convective system.

Figure 3 shows the diabatic moistening rate in the vertical cross section along the line A-B in Fig. 2a. In the EXP1, the region of large negative value of diabatic moistening rate distributes horizontally just under the freezing level, while, in the EXP2, this

feature is not found. The negative value of diabatic moistening rate means condensation of water vapor onto cloud droplets. In Fig. 4, the diabatic heating rate in EXP1 which includes both heating and cooling effects due to condensation and melting shows large positive value in the region corresponding to that of large negative value of diabatic moistening rate in Fig. 3a. Figs. 3 and 4 indicate that condensation growth of cloud droplets is enhanced in the melting layer by the effect of the cooling due to the melting of snow and graupel particles so that, however, the heating due to condensation does not just offset the cooling due to melting, but exceeds it. This means that, in the numerical simulation, the other mechanism than the cooling due to melting should exist to enhance the condensation in melting layer.

4. Discussion and summary

When water saturation has been achieved, the cooling of air due to any processes immediately produces super-saturation to result in condensation. Sub-grid eddy diffusion process also can produce super-saturation, because this process tends to modify the temperature and water vapor profiles to be linear ones while saturated water vapor amount is a non-linear function of temperature. Fig. 5a shows that turbulent kinetic energy (TKE) is distributed where corresponds to the region of the enhancement of condensation. This means that the sub-grid eddy diffusion is effective in the melting layer.

The stability of the air has an important role to produce and maintain the TKE in melting layer. The air tends to become unstable between the cooled layer due to melting and the layer below it. Fig. 5b shows the value of buoyancy term in TKE equation. There is a thin layer which indicates small positive buoyancy or neutral state at about 5-km height in cloud system. In this layer, TKE is enhanced by shear and maintained by the non-negative buoyancy.

Above discussion reveals that the sub-grid eddy diffusion as well as the cooling due to the melting of snow and graupel particles plays a main role to enhance the condensation growth of cloud droplets in the melting layer in our numerical simulation. The simulation result is supposed to be dependant to the grid size and the mixing length in the formulation of sub-grid eddy diffusion, because we applied the parameterization of Klemp and Wilhelmson (1978) and Deardorff (1980). We plan for the further investigation into the sensitivities to grid size and mixing length.

Acknowledgements

This study is conducted by the fund of Research Revolution 2002, and the simulations are made by NEC SX-6 in Meteorological Research Institute.

References

Deardorff, J. W., 1980: Numerical investigation of neutral and unstable planetary boundary layers. *Boundary-Layer Meteorol.*, **18**, 495-527.
 Klemp, J. B. and R. B. Wilhelmson, 1987: The simulation of three-dimensional convective storm dynamics. *J. Atmos. Sci.*, **45**, 1070-1096.
 Saito, K., T. Kato, H. Eito and C. Muroi, 2001: Documentation of the Meteorological Research Institute / Numerical Prediction Division Unified Nonhydrostatic Model. *Tech. Rep. of MRI*, **42**, p133.

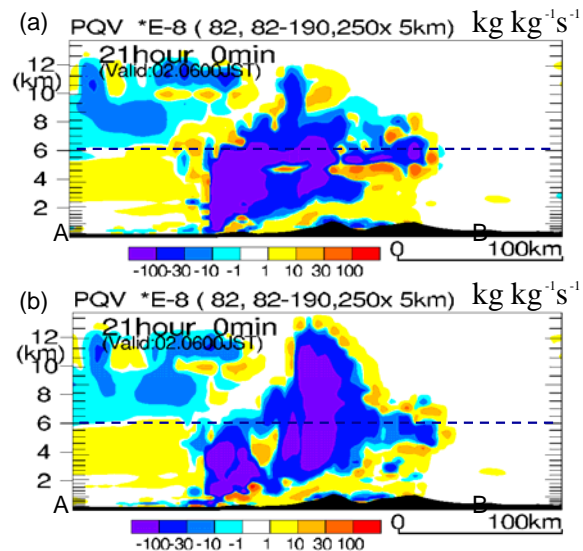


Fig. 3 Diabatic moistening rate in the vertical cross section along the line A-B in Fig. 2a. (a) and (b) correspond to EXP1 and EXP2, respectively. Broken line in each panel indicates the freezing level.

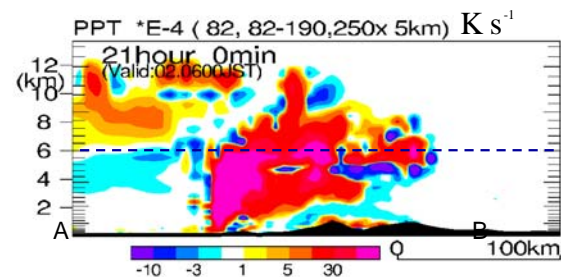


Fig. 4 Same as Fig. 3, but for diabatic heating rate in EXP1.

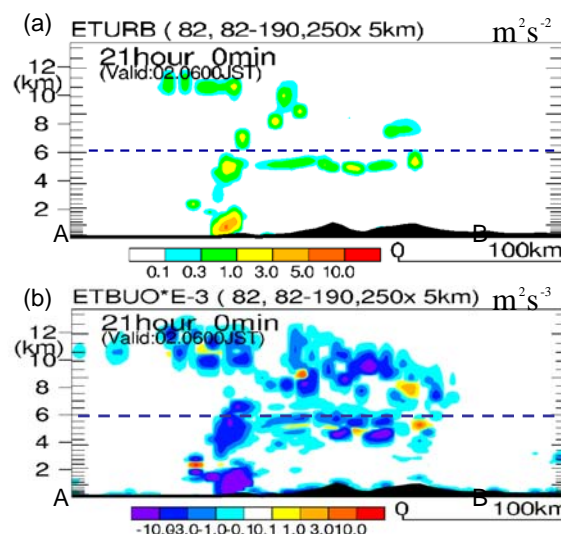


Fig. 5 Same as Fig. 3, but for (a) turbulent kinetic energy (TKE) and (b) buoyancy term in TKE equation in EXP1.

Improvement of a Cloud Ice Fall Scheme in GCM

Hideaki KAWAI*

Climate Prediction Division, Japan Meteorological Agency, Tokyo, Japan

1 Background and problem

A 20km mesh global model (TL959) have been developed by Japan Meteorological Agency and Meteorological Research Institute for the 4th assessment report of Intergovernmental Panel on Climate Change. In the development, a lack of cloud ice content and cloud cover especially at the upper troposphere in TL959 appeared. Some experiments made it clear that the main cause is not a horizontal resolution dependency, but a time step dependency. A time step on physical processes, Δt , in TL959 is 360[s] in contrast to 1800[s] in TL319. Fig. 1 shows that cloud cover is reduced substantially in the case of $\Delta t = 360$ [s].

Generally a treatment of cloud ice falling is a crucial problem in GCM due to its fast fall speed and long Δt . ECMWF IFS CY25r1 type cloud ice fall scheme (ECMWF 2002) was implemented in the model in 2003 to prevent a disappearance of cloud ice at long Δt (Kawai 2003), but this scheme brings a lack of cloud ice at the extremely short time step. The main cause is that a part of cloud ice larger than $100 \mu\text{m}$ is eliminated many times at the shorter time step. The main purpose of the improvement here is to make a flux of larger size cloud ice to be proportional to Δt .

The model is a JMA/MRI unified model and will be used for various researches and operations at a wide variety of resolutions and Δt s. Therefore small timestep dependency is crucially important.

2 Cloud ice fall speed and conversion rate to snow

First, each representative cloud ice fall speed for smaller and larger particles was deduced. Observed size distribution functions of cloud ice (McFarquhar and Heymsfield 1997, hereafter MH97) and size-speed relationships for cloud ice (Heymsfield and Iaquinta 2000) were integrated for its size by the similar procedure to Zurovac-Jevtic and Zhang (2003).

The ice fall speed for ice particles smaller (larger) than $100 \mu\text{m}$, v_{cice} (v_{snow}) [m/s], was obtained as a function of cloud ice concentration smaller (larger) than $100 \mu\text{m}$, $IWC_{<100}$ ($IWC_{>100}$) [kg/m^3], as below (shown in Fig. 3).

$$v_{cice} = 1.56 IWC_{<100}^{0.24} \quad (1)$$

$$v_{snow} = 2.23 IWC_{>100}^{0.074} \quad (2)$$

*e-mail : h-kawai@met.kishou.go.jp

Conversion rate to snow, C_{I2S} [$\text{kg}/\text{kg} \cdot \text{s}$], was deduced using a ratio function of ice particle smaller than $100 \mu\text{m}$ by MH97, $\alpha_{<100}$, as below.

$$C_{I2S} = \frac{1 - \alpha_{<100}}{\alpha_{<100}} \frac{v_{snow}}{H_c} q_{ice} \quad (3)$$

At the deduction, simple assumptions are introduced: (a) concentration of cloud ice is vertically homogeneous, (b) converted snow concentration is accumulate downward, (c) observation altitude of $\alpha_{<100}$ is H_c [km] from a top of a cloud. Here $H_c = 2$ [km] is assumed on the basis of MH97.

3 Procedure of calculation

Prognostic equation of cloud ice is the following, where C_{gnrt} is a source term and $D_{I2S} = C_{I2S}/q_{ice}$.

$$\frac{\partial q_{ice}}{\partial t} = C_{gnrt} + \frac{1}{\rho} \frac{\partial}{\partial z} (v_{cice} \rho q_{ice}) - D_{I2S} q_{ice} \quad (4)$$

1. $\alpha_{<100}$ is calculated using a formula in MH97, v_{cice} from eq. (1), and D_{I2S} from eq.(3) and eq.(2).
2. A snow flux that reaches the ground surface in a moment, \tilde{P}_{snow} [$\text{kg}/\text{m}^2\text{s}$], is calculated as below. The first term in {} of r.h.s. corresponds to a snow which is converted from existing cloud ice, $q_{ice}(t)$, and the second term is a snow which is converted from newly generated cloud ice between t and $t + \Delta t$, $C_{gnrt}\Delta t$, each by the time $t + \Delta t$.

$$\begin{aligned} \tilde{P}_{snow} = & \left\{ \frac{q_{ice}(t)}{\Delta t} (1 - e^{-D_{I2S}\Delta t}) \right. \\ & \left. + (C_{gnrt} - \frac{C_{gnrt}}{D_{I2S}} \frac{1}{\Delta t} (1 - e^{-D_{I2S}\Delta t})) \right\} \rho \Delta z \quad (5) \end{aligned}$$

3. The following analytical solutions of eq. (4) are calculated to obtain $q_{ice}(t + \Delta t)$ using cloud ice inflow flux from the upper layer, R_f [$\text{kg}/\text{m}^2\text{s}$]. $q_{ice}(t)e^{-D_{I2S}\Delta t}$ of eq. (6) corresponds to cloud ice after elimination of snow converted by the time $t + \Delta t$, that is, cloud ice at the time t of analytical solution. The second term of eq. (7) corresponds to newly generated cloud ice which is not converted to snow between t and $t + \Delta t$.

$$\begin{aligned} q_{ice}(t + \Delta t) \\ = q_{ice}(t)e^{-D_{I2S}\Delta t} e^{-D\Delta t} + \frac{C}{D}(1 - e^{-D\Delta t}) \quad (6) \end{aligned}$$

$$C = \frac{R_f}{\rho \Delta z} + \frac{C_{gnrt}}{D_{I2S}} \frac{1}{\Delta t} (1 - e^{-D_{I2S}\Delta t}) \quad (7)$$

$$D = \frac{v_{cice}}{\Delta z} \quad (8)$$

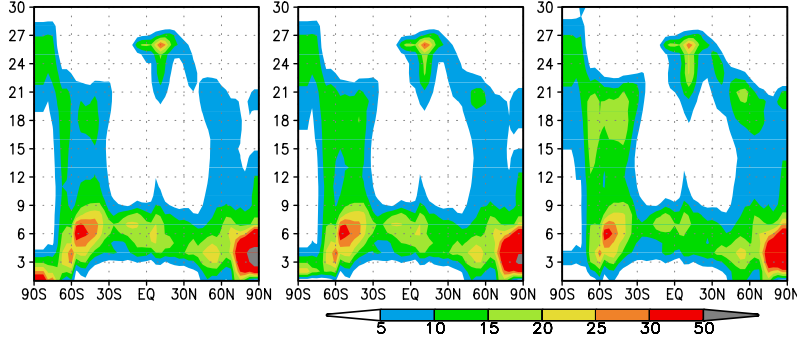


Figure 1. Zonal averaged cloud cover [%] of the original version using TL95. $\Delta t=360, 600, 1800[s]$ from the left side. Vertical axis shows model layer numbers. One week average from the initial time 12UTC 30 Jun 1992.

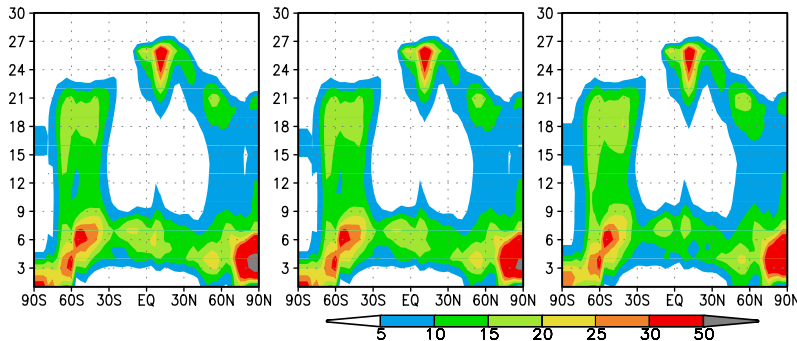


Figure 2. Same as Fig. 1 except for the revised version.

4. A sedimentation flux of cloud ice to lower layers, $R_{f,(k-1)}$, is calculated as the following.

$$R_{f,(k-1)} = \left\{ \frac{q_{ice}(t)e^{-D_{I2S}\Delta t} - q_{ice}(t + \Delta t)}{\Delta t} + C \right\} \rho \Delta z \quad (9)$$

$R_{f,(k-1)}$ is used as R_f of a layer just below the layer at the next loop.

4 Result

Figure 2 shows the result of the revised version. The reduction of upper cloud at short Δt is alleviated by the revised scheme and time step dependency is suppressed. An excess of outgoing longwave radiation flux caused by cloud reduction is also improved (not shown). The increase of cloud cover of tropical anvil is brought by slow fall speed of cloud ice, v_{cice} (eq. (1)).

It is noted that the low cloud cover is less for longer Δt . Larger heating and drying at longer Δt in the cumulus convection process may cause a positive feedback of cloud reduction.

References

European Centre for Medium-Range Weather Forecasts, 2002: IFS Documentation (CY25r1), <http://www>.

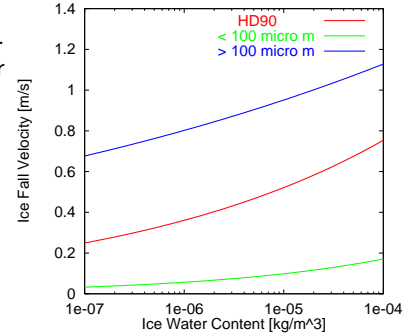


Figure 3. Cloud ice fall speed. v_{cice} of eq. (1) (green line), v_{snow} of eq. (2) (blue), and conventional ice fall speed by Heymsfield and Donner (1990) (red).

ecmwf.int/research/ifsdocs/CY25r1. Part IV, Chapter 6.

Heymsfield, A. J. and L. J. Donner, 1990: A scheme for parametrizing ice-cloud water content in general circulation models. *J. Atmos. Sci.*, **47**, 1865–1877.

Heymsfield, A. J., and J. Iaquinta, 2000: Cirrus crystal terminal velocities. *J. Atmos. Sci.*, **57**, 916–938.

Kawai, H., 2003: Impact of a cloud ice fall scheme based on an analytically integrated solution. *CAS/JSC WGNE Research Activities in Atmospheric and Oceanic Modelling*, **33**, 04.11–12.

McFarquhar, G. M., and A. J. Heymsfield, 1997: Parameterization of tropical cirrus ice crystal size distribution and implications for radiative transfer: Results from CEPEX. *J. Atmos. Sci.*, **54**, 2187–2200.

Zurovac-Jevtic, D. and G. J. Zhang, 2003: Development and Test of a Cirrus Parameterization Scheme Using NCAR CCM3. *J. Atmos. Sci.*, **60**, 1325–1344.

Development of a subgrid scale parameterisation of mountain glaciers for use in regional climate modelling

Sven Kotlarski, Daniela Jacob
Max Planck Institute for Meteorology, Hamburg, kotlarski@dkrz.de

Introduction

The proper description of cryospheric processes is essential for simulating the complete terrestrial water cycle in climate models. Besides the large polar ice sheets, this is especially true for alpine river catchments where the regional climate as well as seasonal runoff patterns are strongly influenced by the presence of glaciers (SINGH and SINGH, 2001; JANSSON et al, 2003). In order to simulate the two-way interaction between glaciers and climate, existing models for both components have to be merged. So far, the terrestrial cryosphere is represented in an extremely simplified way in most state-of-the-art global and regional climate models (GCM and RCM). Static glacier maps are used indicating whether a specific climate model grid box is covered by land ice or not. These maps remain constant throughout the model integration and the glacierised surface area is kept unchanged even in case of pronounced snow accumulation or melting of snow and ice. Furthermore, runoff generation is usually neglected over ice covered areas.

This simple approach is suitable for short model integrations and for large ice sheets with a slow response to climatic forcing. For longer simulations and especially for assessing regional climate change effects and its impacts on runoff regimes in alpine regions, a more detailed description of processes related to mountain glaciers is required. Therefore, a subgrid scale parameterisation of mountain glaciers is being developed and implemented into the regional climate model REMO (JACOB, 2001). The new scheme expands and partly replaces the static glacier mask used so far and includes the most important processes governing the extent of mountain glaciers and their potential influence on regional climate and runoff conditions.

The New Mountain Glacier Scheme

In order to account for glacierised surfaces on a subgrid level, land ice is introduced as a fourth possible surface fraction of a REMO grid box in addition to ice-free land, water and sea ice. The sum of all four sub areas equals the total grid box area. Turbulent surface fluxes are derived separately for each fraction by applying a bulk transfer relation with transfer coefficients derived from Monin-Obukhov similarity theory. Fluxes are subsequently averaged within the lowest atmospheric level using the corresponding surface fractions as weights (*tile approach*).

The total land ice mass of a specific grid cell is represented by one single glacier covering a certain fraction of the total grid box land area (Fig. 1). The glacial body consists of two layers: a surface layer of 10 cm thickness and a bottom layer representing the main ice mass. Both the glacierised and the non-glacierised surface fraction can be covered by a snow layer and share a common soil consisting of five temperature layers. The surface albedo of glacier ice is a linear function of ice temperature of the upper layer and varies between 0.4 ($T_{ice} \leq -10^{\circ}\text{C}$) and 0.3 ($T_{ice} = 0^{\circ}\text{C}$). Meltwater of the upper ice layer directly contributes to surface runoff while meltwater originating from the bottom layer is an additional water input for the soil surface and is subsequently divided into surface

runoff and infiltration. So far, no additional storage or refreezing of meltwater within the ice is implemented.

Snow on the glacierised and non-glacierised surface fractions can be transformed into glacier ice once a continuous snow cover of 730 days is reached. In order to account for the fact that within a REMO grid box glaciers are assumed to be located at higher altitudes (= lower mean air temperature) rather than in lowland areas, a part of the total grid box snow fall rate is redistributed from the non-glacierised surface fraction to the glacier. Ice flow processes within a grid box are not explicitly accounted for. Instead, the size of the glacierised area is controlled by a simple volume area relation which is based on a power law (BAHR et al., 1997):

$$V = c * A^{\gamma} \quad (1)$$

with glacier volume V [m^3] and glacier area A [m^2]. The constant c and the scaling parameter γ are taken from CHEN and OHMURA (1990) who tuned c to 0.206 and γ to 1.357 based on data from 63 alpine glaciers. Ice flow between adjacent grid boxes is totally neglected in the presented parameterisation. Glaciers in neighbouring grid cells do not interact directly which restricts the usage of the new scheme to mountain glaciers and small ice caps where large scale ice flow processes can be neglected.

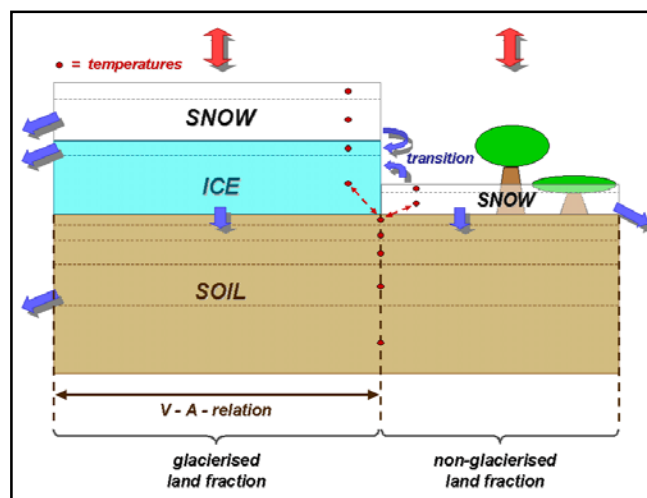


Fig. 1: Schematic overview of the new mountain glacier scheme.

Experimental Setup

A first 10-year test simulation for the period 1979-1988 has been performed using REMO version 5.3 with the fully coupled mountain glacier scheme. The regional model domain covers the European Alps with a horizontal resolution of $1/6^{\circ}$ (approx. 18×18 km grid box size) and 20 vertical levels. Lateral forcing as well as atmospheric initial conditions are provided by a REMO $1/2^{\circ}$ simulation which in turn is driven by ERA15 reanalysis (double nesting technique). Initial ice temperatures were set to 0°C for the entire domain. Glacierised area and mean ice depth for the single REMO boxes were initialised using data of the World Glacier Inventory (NSIDC, 1999). The resulting glacierised surface fraction at initialisation is lower than 10% for most grid cells

However, maximum values of up to 50% are reached in the Swiss Alps, where maximum mean ice depth lies between 90 and 100 m icepack (not shown).

Results

After 10 years of model simulation, almost all grid cells show a decrease of glacierised area (Fig. 2). The relative decrease is largest in grid cells with a low grade of glaciation in 1979 and reaches up to 100% (total disappearance of glaciers). The larger the ice covered area at initialisation, the smaller the relative loss of area. This is at least in parts a direct effect of the larger volume-to-surface ratio of highly glacierised boxes due to the positive relationship between glacier area and ice depth derived from eq. (1). Three REMO boxes, however, show a slight increase of glacierisation (up to 8%). The overall decrease of ice covered area in the model domain between January 1979 and December 1988 is -45.5%, which is too high compared to observed area changes. PAUL et al. (2004) estimate a relative decrease of glacier area in the Alps of only 22% for the period 1973-1999, including the stabilisation period until 1985 and a strong retreat thereafter.

In order to verify ongoing processes and to find possible reasons for too high melt rates, two REMO grid cells have been analysed in more detail. These boxes are located in the western part of the Alps and have an initial degree of glaciation of 22.5% and 33.6% respectively (Fig. 3 a). After 10 years of continuous simulation, the glacierised area fraction of box A decreased down to 10.9% (-51.6%) while Box B shows a slight increase of ice cover (+0.6%). The pronounced melting of snow and ice in Box A leads to mean monthly runoff peaks of > 40 mm/day in summertime (Fig. 3 b). The presence of snow on top of the ice surface throughout the whole year in box B (Fig. 3 c) also prevents the ice from being melted which at least partially explains the stable ice volume in this grid cell. A further reason for the pronounced melt rates in box A is the higher amount of net surface radiation in summertime with energy input exceeding 100 W/m² (Fig. 3 d). This is partly due to the disappearance of snow in summer which exposes the darker ice surface and increases absorption of solar radiation via decrease of surface albedo. The surface sensible heat fluxes are positive throughout most parts of the year (energy flux from air to surface) but only reach maximum values of about 45 W/m² (Fig. 3 e) which is small compared to radiation fluxes. We

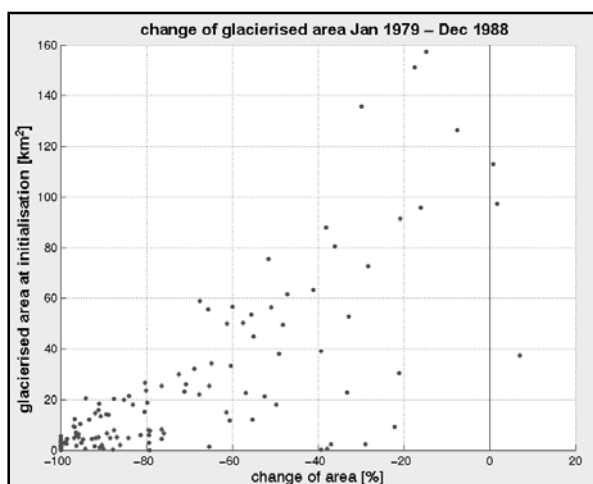


Fig. 2: Change of glacierised area [%] after 10 year model simulation (each dot represents a single REMO grid box).

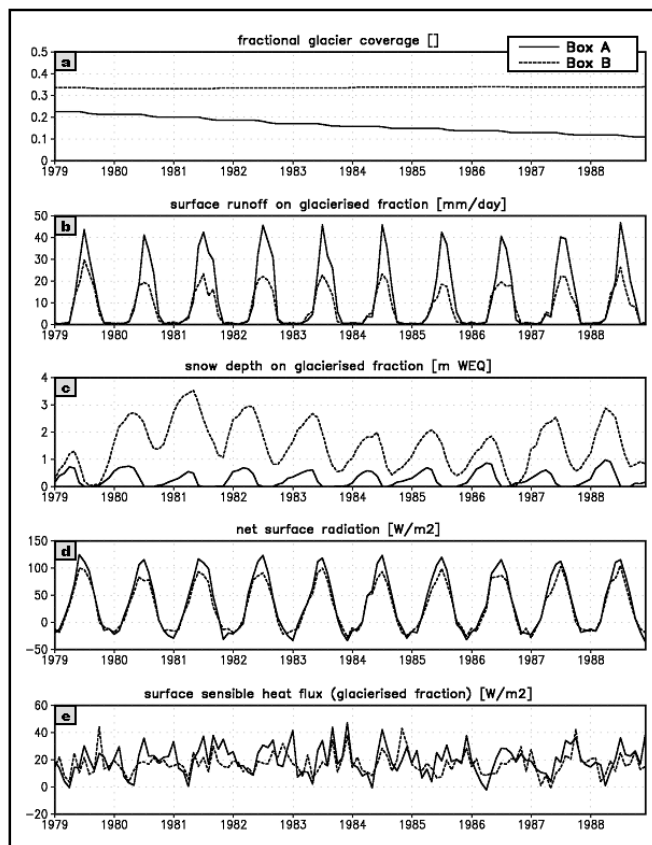


Fig. 3: Evolution of different surface parameters for grid boxes A and B throughout the 10-year simulation period (monthly mean values).

therefore assume that the reason for too high melt rates throughout the model domain lies in processes connected to radiation and in the internal distribution of temperature within the glacier rather than in too high air temperatures (caused for example by the neglect of subgrid scale orography). However, both possibilities will be investigated in more detail in the near future. A special regard will be paid to comparison of simulated and observed air temperatures above glacierised surfaces.

References

- BAHR, D., MEIER, M., PECKHAM, S. (1997): The physical basis of glacier volume-area scaling. *J. Geophys. Res.* 102: 20 355 – 20 362.
- CHEN, J. and OHMURA, A. (1990): Estimation of Alpine glacier water resources and their changes since 1870s. In: *Hydrology in Mountainous Regions. I – Hydrological Measurements; the Water cycle.* IAHS publ. 193: 127-135.
- JACOB, D. (2001): A note to the simulation of the annual and inter-annual variability of the water budget over the Baltic Sea drainage basin. *Meteorol. Atmos. Phys.* 77, 61-73.
- JANSSON, P., HOCH, R., SCHNEIDER, T. (2003): The concept of glacier storage: a review. *J. Hydrol.* 282, 116-129.
- NSIDC (1999). World Glacier Inventory. World Glacier Monitoring Service and National Snow and Ice Data Center/World Data Center for Glaciology. Boulder, CO. Digital media: http://nsidc.org/data/glacier_inventory
- PAUL, F., KÄÄB, A., MAISCH, M., KELLENBERGER, T., HAEUBLI, W. (2004): Rapid disintegration of Alpine glaciers observed with satellite data. *Geophys. Res. Lett.* 31, No. 21, L21402.
- SINGH, P. and SINGH, V. (2001): *Snow and glacier hydrology.* Kluwer Academic Publishers, 742 pp.

Inclusion of an urban canopy parameterization in the Canadian meteorological models

A. Lemonsu^{1†}, S. Bélair[†] and J. Mailhot[†]

[†] Environment Canada, Meteorological Service of Canada, Meteorological Research Branch,
2121 TransCanada Highway, Dorval, Quebec H9P 1J3 , Canada

1. Introduction

The current meteorological models can be run at high horizontal resolutions reaching a few hundreds of meters. At such scales, the cities cover several grid points and the impact of the urban radiative, energetic, dynamic and hydrological effects must be taken into account in the computation of the surface exchanges. Specific urban canopy schemes have been recently developed in order to parameterize the exchanges between the urban covers and the atmosphere and implemented in atmospheric mesoscale models, e.g. the models of Mills (1997) and Martilli et al. (2002). The Town Energy Balance scheme (TEB) (Masson, 2000) is part of this new generation of models. It is already coupled to the French community research atmospheric model Meso-NH (Lafore et al., 1998) and was recently included in the physics package of the Global Environmental Multiscale (GEM) and the Mesoscale Compressible Community (MC2) Canadian models.

2. Presentation of TEB

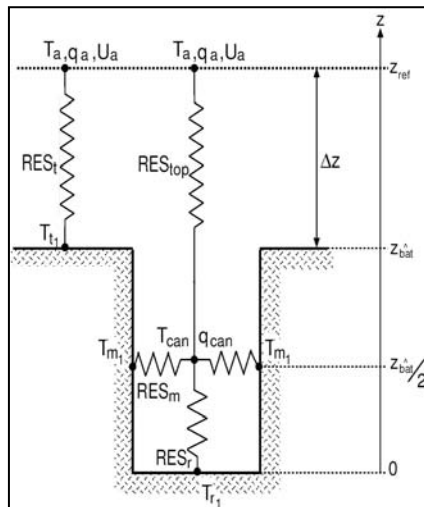


Figure 1: The TEB urban surface scheme.

TEB is an urban canopy model based on the concept of urban canyon (Nunez and Oke, 1977). At each mesh of the model is associated one single street canyon composed of three simple elements, namely one horizontal road, two identical vertical walls and one roof (Figure 1). The canyon is described by a set of input data: geometric parameters (mean building height, dynamical roughness length of the urban canopy, building density, aspect ratio of the street and ratio between the vertical surfaces and the plane built area) and radiative and thermal properties of materials (albedos, emissivities, heat capacities and thermal conductivities) for each of the surfaces. Thus, this canyon corresponds to an average of all the streets of the grid mesh. TEB applies two major assumptions: (1) the orientation of the streets is isotropic; and (2) the intersections are neglected. Given the fact that the microscale effects are different for each urban surface, TEB computes the radiative, energetic and water exchanges independently for the road, the walls and the roof.

Finally, by using a simplified but realistic description of the urban geometry, TEB is especially well adapted to mesoscale modeling. It was already evaluated in offline mode on various kinds of urban sites (Masson et al., 2002; Lemonsu et al., 2004) and applied to 3D modelling exercises (Lemonsu and Masson, 2002; Lemonsu et al., 2005).

3. Implementation of TEB

Initially, the physics package of GEM and MC2 decomposes the surface as 4 distinct types of covers: land surfaces with vegetation, open waters, ice-covered waters and glaciers. Each of them is treated by a specific parameterization. The implementation of TEB in the physics package required the inclusion of a fifth type of cover associated with the built-up areas. Most of the input data describing the urban canyons are determined according to the land use cover classification (next section). The prognostic variables such as surface temperatures, air temperature and humidity inside the canyons are initialized by using analyses or forecasts. At each grid point, the surface outputs are

¹ E-mail: aude.lemonsu@ec.gc.ca

aggregated according to the fraction of each type of covers, especially the energy and momentum fluxes which are required to force the atmospheric model. To evaluate the impact of the urban parameterization on the response of the atmospheric model, simple meteorological situations of the Joint Urban 2003 experiment (Oklahoma City, US) will be simulated with MC2 and TEB.

Urban classes			
1	High Buildings	7	Roads and parking lots
2	Mid-high buildings	8	Road borders
3	Low buildings	9	Dense residential
4	Very low buildings	10	Mid-dense residential
5	Industrial areas	11	Low-dense residential
6	Sparse buildings	12	Mix of nature and built

Table 1: Identification of the 12 urban classes.

As for the soil-vegetation-atmosphere transfer (SVAT) models, the TEB input data are associated with a land use cover classification. Since most of the databases do not include urban classes, a general methodology has been developed to produce urban classifications in a semi-automatic way for the major North American cities. It is based on the pre-analysis of digital elevation models (DEM) and of ASTER satellite imagery providing a classification in simple elements (i.e. road, roof, tree etc) at 15-m horizontal resolution. Afterwards, an aggregation process and a decision tree classification lead to a 60-m database of 12 urban classes (Table 1). The sets of parameters associated with each class are defined from the analysis of aerial photograph samplings and the use of literature tables and previous study results (Masson et al., 2003). A first classification was established for Oklahoma City.

Acknowledgements

This work is conducted in the frameworks of the CBRN (Chemical, biological, radiological, and nuclear agents) Research and Technology Initiative (CRTI) Project #02-0093RD managed by Environment Canada (CMC/MRB), Defense R&D Canada, Health Canada and Atomic Energy Canada. It is funded by a postdoctoral fellowship from the National Science in Engineering Research Council (NSERC).

References

- Lafore J.P., J. Stein, N. Asencio, P. Bougeault, V. Ducrocq, J. Duron, C. Fischer, P. Hérelil, P. Mascart, V. Masson, J.P. Pinty, J.L. Redelsperger, E. Richard and J. Vila-Guerau de Arellano, 1998: The Méso-NH atmospheric simulation system. Part I: Adiabatic formulation and control simulation. *Ann. Geophys.*, **16**, 90-109.
- Lemonsu A. and V. Masson, 2002 : Simulation of a summer urban breeze over Paris, *Boundary-Layer Meteorol.*, **104**, 463-490.
- Lemonsu A., C.S.B. Grimmond and V. Masson, 2004: Simulation of the Energy Budget of an old mediterranean city core, *J. Appl. Meteorol.*, **43**, 312-327.
- Lemonsu A., G. Pigeon, V. Masson, P. Durand and C. Moppert, 2005: Sea-town interactions over Marseille : 3D Urban Boundary Layer structure and thermodynamic fields near the surface, *Theoretical and Appl. Climatology*, accepted.
- Martilli A., A. Clappier and M.W. Rotach, 2002: An urban surface exchange parameterization for mesoscale models. *Boundary-Layer Meteorol.*, **104**, 261-304.
- Masson V., 2000: A physically-based scheme for the urban energy budget in atmospheric models. *Boundary-Layer Meteorol.*, **94**, 357-397.
- Masson V., C.S.B. Grimmond and T.R. Oke, 2002: Evaluation of the Town Energy Balance (TEB) scheme with direct measurements from dry districts in two cities. *J. Appl. Meteorol.*, **41**, 1011-1026.
- Mills G., 1997: An urban canopy-layer climate model. *Theoretical and Appl. Climatology*, **57**, 229-244.
- Nunez M. and T.R. Oke, 1977: The energy balance of an urban canyon, *J. Appl. Meteorol.*, **16**, 11-19.

Implementation of a Lake Model FLake into the Limited-Area NWP System LM of the German Weather Service: Preliminary Results

Dmitrii Mironov^{1}, Natalia Schneider², Bodo Ritter¹ and Erdmann Heise¹*

¹ German Weather Service, Offenbach am Main, Germany

² University of Kiel, Kiel, Germany

A recently developed lake model (Mironov et al. 2003, 2004) for use in NWP, climate modelling and other numerical prediction systems for environmental applications is implemented into the limited-area NWP system LM (Steppeler et al. 2003) of the German Weather Service (DWD) and first test runs are performed. The lake model, termed FLake, is a bulk model based on a parametric self-similar representation (assumed shape) of the evolving temperature profile. A detailed description of FLake is given in Mironov (2004). Some results from single-column numerical experiments with FLake are presented in Mironov et al. (2003, 2004). The most important finding from the single-column experiments is that the results are not too sensitive to changes in external parameters except for the lake depth.

In order to be incorporated into an NWP system, FLake requires a number of two-dimensional external-parameter fields. These are, first of all, lake fractions (area fraction of a given LM grid box covered by lake water that must be compatible with the land-sea mask used) and lake depths. A two-dimensional lake-fraction field for the LM domain used operationally at DWD is developed on the basis of a Global Land Cover Characterization (GLCC) data set (<http://edcdaac.usgs.gov/glcc>) with 30 arc sec resolution, that is ca. 1 km at the equator. A lake-fraction field for the DWD LM domain is shown in Fig. 1. A data set containing mean depths of a number of European lakes and of a few lakes from other regions of the world is developed at DWD. On the basis of that data set, the lake-depth external-parameter field is developed for the DWD LM domain (not shown). Since no tile approach is used in LM (i.e. each LM grid-box is characterised by a single land-cover type), only the grid-boxes with the lake fraction greater than 0.5 are treated as lakes. Each lake is characterised by its mean depth. Other external parameters, e.g. optical characteristics of the lake water, are assigned their default values offered by FLake.

Using the above external-parameter fields, an extended version of LM that incorporates FLake is tested through parallel experiments including the LM data assimilation cycle. In the present simplest configuration, the heat flux through the water-sediment interface is set to zero and a layer of snow over the lake ice is not considered. The effect of snow above the ice is accounted for parametrically through changes in the surface albedo with respect to solar radiation (cf. Mironov and Ritter 2004). Surface fluxes of momentum and of sensible and latent heat are computed with the operational LM surface-layer parameterization scheme (Raschendorfer 2001). Optionally, a new surface-layer scheme can be used that accounts for specific features of the surface air layer over lakes. First results from parallel runs (not shown) look reasonable. Further comprehensive testing of FLake and comparison of results from parallel experiments with LM-FLake with observational data are required. The work is underway at DWD.

In the future, efforts should be taken to considerably extend the data set of lake depths that should eventually cover the entire globe. The task is by no means trivial considering the scarcity of available information. A more detailed information on the lake area coverage may also be needed. For example, the land cover type “inland water” used in the GLCC data set does not distinguish between lakes and rivers. Then, river points should be removed from the

*Corresponding author address: Deutscher Wetterdienst, AP2003, Kaiserleistr. 29/35, D-63067 Offenbach am Main, Germany. E-mail to dmitrii.mironov@dwd.de.

lake-fraction field prior to its use with FLake. A number of such false lake points are seen in Fig. 1. This is not a serious problem for the LM operational at DWD, where the horizontal grid-size is ca. 7 km and no tile approach is used to describe the land cover within a given grid box. The problem will become more serious as the resolution is increased and/or the tile approach is used. The external parameters other than lake fraction and lake depth may also be refined as more information becomes available.

Acknowledgements. The work was partially supported by the EU Commission through the project INTAS-01-2132.

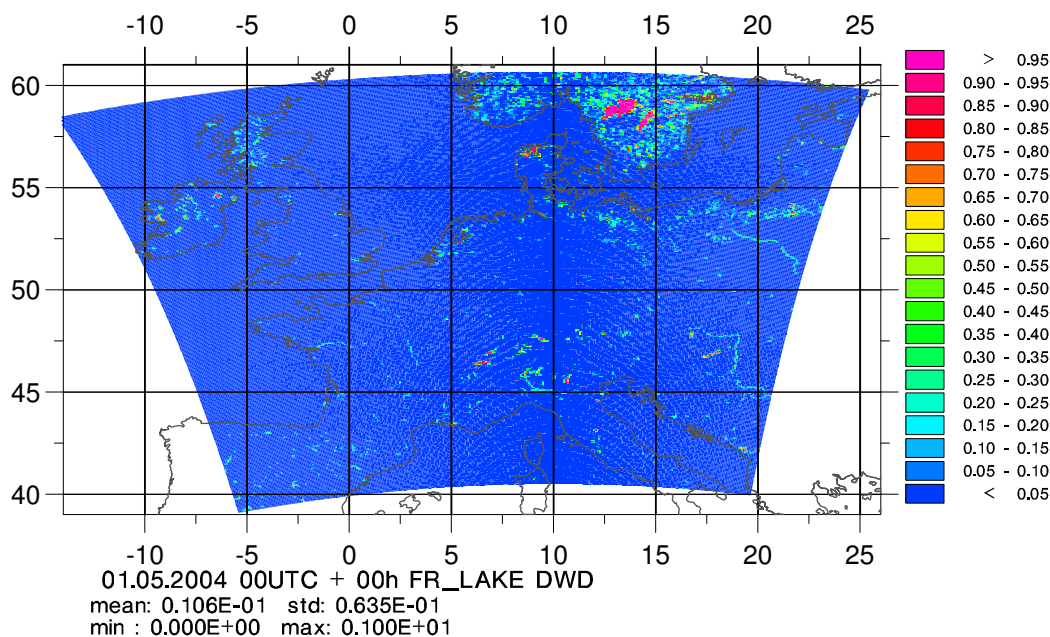


Figure 1. Lake fraction for the LM domain used operationally at DWD.

References

- Mironov, D. V., 2004: Parameterization of lakes in numerical weather prediction. Part 1: Description of a lake model. Deutscher Wetterdienst, Offenbach am Main, Germany. (manuscript is available from the author)
- Mironov, D., and B. Ritter, 2004: Testing the new ice model for the global NWP system GME of the German Weather Service. *Research Activities in Atmospheric and Oceanic Modelling*, J. Côté, Ed., Report No. 34, April 2004, WMO/TD-No. 1220, 4.21–4.22. (http://www.cmc.ec.gc.ca/rpn/wgne/2004/individual-articles/04_Mironov_Dmitrii_DMBR_bluebook_04.pdf)
- Mironov, D., A. Terzhevik, F. Beyrich, and E. Heise, 2004: A Lake Model for Use in Numerical Weather Prediction Systems. *Research Activities in Atmospheric and Oceanic Modelling*, J. Côté, Ed., Report No. 34, April 2004, WMO/TD-No. 1220, 4.23–4.24. (http://www.cmc.ec.gc.ca/rpn/wgne/2004/individual-articles/04_Mironov_Dmitrii_MTBH_WMOBlueBook04.pdf)
- Mironov, D., A. Terzhevik, F. Beyrich, E. Heise, and H. Lohse, 2003: A two-layer lake model for use in numerical weather prediction. *Proc. of the Baltic HIRLAM Workshop*, 17 – 20 November 2003, St. Petersburg, Russia, 83–85. (<http://hirlam.fmi.fi/Baltic/bhws/report/p083.pdf>)
- Raschendorfer, M., 2001: The new turbulence parameterization of LM. *COSMO Newsletter*, No. 1, 89–97. (<http://cosmo-model.cscs.ch>)
- Stappeler, J., G. Doms, U. Schättler, H. W. Bitzer, A. Gassmann, U. Damrath, and G. Gregoric, 2003: Meso-gamma scale forecasts using the non-hydrostatic model LM. *Meteorol. Atmos. Phys.*, **82**, 75–96.

Introduction of a New Radiation Scheme to the Operational Global NWP Model at JMA

Shigeki MURAI, Syoukichi YABU

Japan Meteorological Agency

1-3-4 Otemachi, Chiyoda-ku, Tokyo 100-8122, JAPAN

e-mail : murai@met.kishou.go.jp, yabu@met.kishou.go.jp

1 Introduction

The operational Global Spectral Model (GSM) at JMA has warming bias in the upper stratosphere and cooling bias in the lower stratosphere, and underestimates the downward longwave flux at the ground. It is considered that low accuracy of the radiation scheme causes most of these errors. JMA has developed a new radiation scheme to reduce the errors. As it was confirmed that the forecast skill of GSM improved with the new scheme, it has been in operation since 2 December 2004.

2 Outline of the new scheme

Longwave spectrum is divided into 9 bands and the radiation flux is calculated in each band separately. Considering a tradeoff between accuracy and efficiency, gaseous transmittance is computed using three different approaches, depending on the absorber and the spectral band.

In order to take account of the Doppler absorption effect accurately, a table look-up method (Yabu 2003) is used for spectral bands contributing cooling in the stratosphere. It is accurate enough to calculate transmission functions though it is computationally expensive.

For calculating the other line absorptions, a k-distribution method with linear pressure scaling based on Chou et al. (2001) is used. The scaling parameters are decided to calculate heating rate properly compared with results by a line-by-line method.

A parameterization of water vapor continuum absorption is also revised. The old scheme uses parameterization of Roberts et al. (1976) and takes account of only e-type absorption. The new scheme is based on Zhong and Haigh (1995), which can deal with the effect of P-type absorption. In our parameterization, absorption coefficients are fitted by using the MT-CKD continuum model.

Effects of absorption by trace gases such as CH₄, N₂O and CFCs are newly introduced into the longwave calculation.

In addition to above changes in the longwave scheme, the absorption coefficient parameterization for CO₂, O₂ and O₃ is refined in the new shortwave scheme.

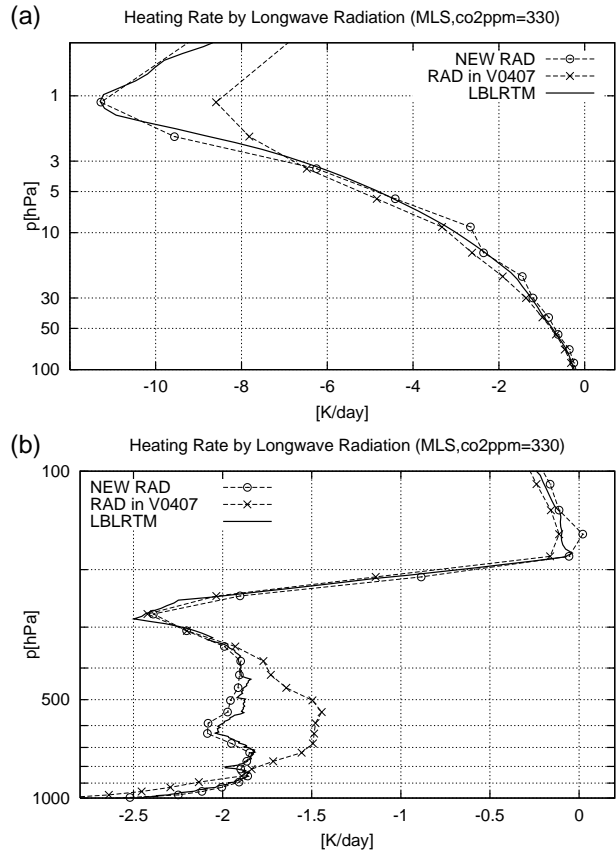


Figure 1. Heating rate by longwave radiation for the midlatitude summer profile by the old scheme (×), the new scheme (○) and the line-by-line method (solid line) (a) above 100hPa, (b) below 100hPa.

3 Characteristic of the scheme

Figure 1 shows the longwave heating rate profiles calculated for the midlatitude summer profile. The old scheme underestimates the cooling around the stratopause (near 1hPa in Figure 1(a)), and the new scheme reduces the error. This change is brought mainly by taking account of the Doppler absorption effect properly. Heating rate profiles for the troposphere are shown in Figure 1(b). The old scheme underestimates the cooling in the middle troposphere and overestimates near the surface. These errors are reduced by the revision of transmittance calculation of line absorptions and the introduction of P-type absorption.

The old scheme underestimates the downward long-

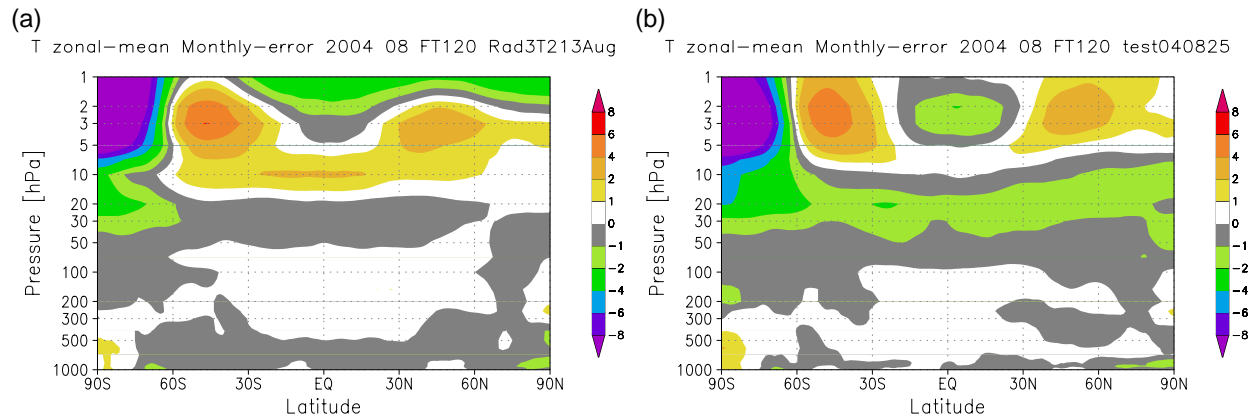


Figure 2. (a) Zonal mean temperature bias for 5-day forecasts by the new scheme. (b) Same as (a) but by the old scheme. Unit is K.

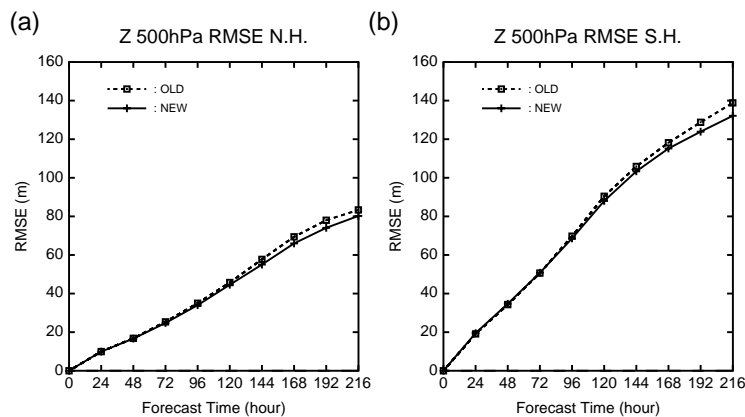


Figure 3. RMSE of the 500hPa geopotential height for August 2004 (a) over the northern hemisphere, (b) over the southern hemisphere.

wave flux at the surface over the nearly whole globe. Flux expressed by the new scheme increases especially over the tropical region and over land. A difference between forecasts and the Surface Radiation Budget (SRB; WCRP-96 1992) is smaller than 10 W/m^2 over the wide area. Overestimation of outgoing long-wave radiation (OLR) is also reduced (not shown).

4 Forecast performance of the model

To confirm the impact of the scheme on forecasts, data assimilation and forecast experiments were carried out for January and August 2004.

Figure 2 shows the zonal mean temperature bias for 5-day forecasts. The old scheme has cooling bias over 2K near 20hPa level while the forecasts by the new scheme reduces the bias to 1K or less.

Figure 3 compares the root mean square error (RMSE) of the geopotential height at 500hPa over the northern and southern hemispheres for the experiment of August 2004. The new scheme (solid) improves the objective scores compared with the old scheme (dashed) over both hemispheres.

References

- Chou, M.-D., M. J. Suarez, X.-Z. Liang and M. M.-H. Yan, 2001: A thermal infrared radiation parameterization for atmospheric studies. *Technical Report Series on Global Modeling and Data Assimilation*. NASA Tech. Mem. **19**, 56pp.
- Roberts, R. E., J. E. A. Selby and L. M. Biberman, 1976: Infrared continuum absorption by atmospheric water vapor in the $8\text{-}12 \mu\text{m}$ window. *Appl. Opt.*, **15**, 2085–2090.
- Yabu, S, 2003: The Doppler absorption in the thermal infrared radiation parameterization of JMA Global Spectrum Model. *CAS/JSC WGNE Research Activities in Atmospheric and Oceanic Modelling*, **33**, 04.29–30.
- Zhong, W. and J. D. Haigh, 1995: Improved broadband emissivity parameterization for water vapor cooling rate calculations. *J. Atmos. Sci.*, **52**, 124–138.
- WCRP-96, 1992: Radiation and climate: Report of the fourth session of the WCRP working group on radiative fluxes. WMO/TD-No.471.

A Comparison of In-cloud and Environmental Properties in Numerical Results between Cloud-resolving and Parameterized Simulations for a Tropical Cyclone Rainband

Akihiko MURATA and Mitsuru UENO

Meteorological Research Institute / Japan Meteorological Agency, Tsukuba, Ibaraki 305-0052, Japan
(corresponding author: amurata@mri-jma.go.jp)

1. Introduction

Precipitation in a tropical cyclone appears to be sensitive to the formulation for cumulus parameterization because latent heat release is a key factor for tropical cyclone intensification. Smith (2000) pointed out that the details of tropical cyclone evolution seemed to be sensitive to the treatment of convection in numerical models. We also showed that representation of a prominent rainband in a tropical cyclone was sensitive to the choice of cumulus parameterization (Murata et al. 2003).

Recently, we investigated the vertical profiles of fractional entrainment rate as to cumulus convection (Murata and Ueno 2003). Numerical simulations of a tropical cyclone rainband were conducted using a high-resolution three-dimensional cloud-resolving model (CRM) with the 200-m horizontal resolution. Fractional entrainment rate, derived from the calculation based on the vertical gradient of cloud mass flux, showed larger near cloud base and top. Entrainment rate was smaller in between and was even negative in many cases that suggested laterally detrained air from a cumulus into the environment.

In this study, on the basis of the results of the CRM simulations, vertically variable entrainment rate is applied to the Arakawa-Schubert (AS) cumulus parameterization. We then compare in-cloud and environmental properties in the result of a parameterized simulation for a tropical cyclone rainband to that of a cloud-resolving simulation.

2. Formulation of entrainment rate in the modified scheme

We modify the formulation of entrainment rate in a version of AS scheme operationally used in Japan Meteorological Agency, which has the prognostic equation that predicts the cloud-base mass flux and has a downdraft and a mid-level convection (Kuma et al. 1993). The modified version adopts vertically variable entrainment rate that represents larger values near cloud base and top, instead of vertically constant entrainment rate used in the original version. The rate has negative values, representing lateral detrainment, in a part of the cloud layer. Detrainment at cloud top, same as the original version, is also included.

Firstly, for each cloud spectrum, we prescribe the lateral detrainment layer and set the heights of the base, z_{DB} , and top, z_{DT} , of the layer. Below the base, the vertical profile of entrainment rate, λ , should increase with height, z . For simplicity's sake, we assume an equation of cloud mass flux, M , as follows: $M/M_B = az^2 + bz + c$ ($z_B < z < z_{DB}$), where the subscript B denotes cloud base and a , b and c are constants determined from following conditions: $\lambda = \lambda_B$ at $z = z_B$ and $\lambda = 0$ at $z = z_{DB}$, where λ_B is entrainment rate at the height of cloud base, z_B . Above the base of the detrainment layer, entrainment rate is assumed as follows: $\lambda = \lambda_D$ ($z_{DB} < z < z_{DT}$), λ_T ($z_{DT} < z < z_T$), where λ_D (< 0) denotes the effect of lateral detrainment. The constants, z_{DB} , z_{DT} , λ_B , and λ_D , are determined on the basis of the results of the CRM simulations. The remaining constant, λ_T , is automatically determined so that the following condition is satisfied: cloud top height is located where buoyancy in the cumulus disappears. This is the same condition as that adopted in the original AS scheme.

3. Comparison of properties in convective updrafts between the results of cloud-resolving and parameterized simulations

The Meteorological Research Institute / Numerical Prediction Division nonhydrostatic model (MRI/NPD-NHM; Saito et al., 2001) is used for comparison of the results between cloud-resolving (200-m horizontal grid spacing) and parameterized (20-km horizontal grid spacing) simulations for a rainband in typhoon Saomai (2000). Compared variables in convective updrafts are cloud mass flux, moist static energy and specific humidity.

The vertical profile of cloud mass flux, normalized by the value at cloud base, obtained by the simulation with the modified scheme is more consistent with that of the cloud-resolving simulation, compared to that obtained by the simulation with the original scheme. The mass flux in the cloud-resolving experiment has the maximum at 4.5 km high and increases rapidly from cloud base to 2-km high (Fig.1). The features are consistently reproduced by the modified scheme, although the peak value is slightly larger than that produced by the CRM one and the

values above 5.5-km high is overestimated. The mass flux reproduced by the original scheme, on the other hand, increases linearly from cloud base to top, which is completely different from that obtained by the CRM.

Thermodynamic properties reproduced by the modified scheme are also more consistent with those in the CRM result. From a comparison of moist static energy (Fig.2), it is found that the rapid decrease in the quantity from cloud base to 3-km high and vertical uniformity between 3- and 6-km high are represented well in the simulation with the modified scheme, although the absolute values are larger than that in the cloud-resolving experiment. Underestimates of specific humidity above 5-km high, shown in the experiment with the original scheme, is slightly improved (Fig.3).

4. Comparison of environmental properties between the results of cloud-resolving and parameterized simulations

Thermodynamic properties in the environment is more consistent with those produced by the CRM when we use the modified scheme, where the term “environment” refers to grid-scale for the parameterized simulations and refers to an average of 100x100 horizontal grid points, corresponding to the 20-km resolution, for the cloud-resolving simulation.

The vertical profiles of moist static energy and specific humidity in the simulation with the modified scheme approach those of the CRM result, suggesting the reduction of underestimates in the quantities (Fig.4 and 5). In particular, noticeable improvement is evident from middle to upper troposphere than below. The result suggests that cloud mass fluxes at those levels are suppressed owing to lateral detrainment, which reduces the mass fluxes above. The improvement, on the other hand, is insufficient in the lower troposphere, indicating that the cloud mass flux there is still too large. To improve the profile of cloud mass flux, it is necessary to verify arbitrary parameters in the modified scheme.

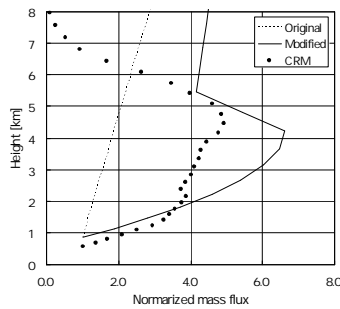


Fig.1 Vertical profiles of normalized cloud mass flux in a convective cloud in a rainband obtained by the parameterized model with the original and modified AS scheme and by the CRM.

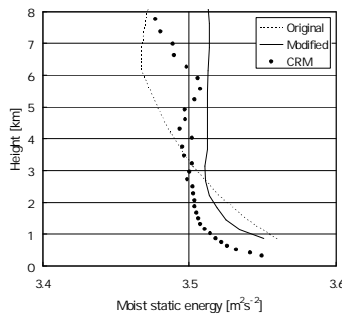


Fig.2 Same as in Fig.1, but moist static energy.

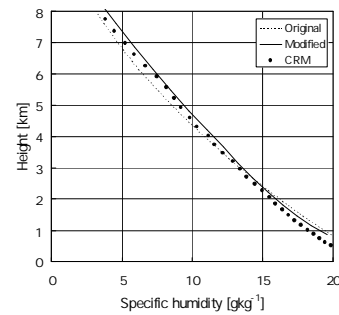


Fig.3 Same as in Fig.1, but specific humidity.

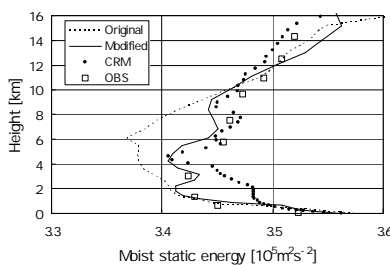


Fig.4 Vertical profiles of environmental moist static energy in a rainband obtained by the parameterized model with the original and modified AS scheme and by CRM. Observational data at the island of South-Daito are also plotted.

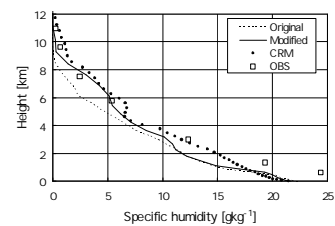


Fig.5 Same as in Fig.4, but specific humidity.

References

- Kuma, K., C.-H. Cho, C. Muroi and M. Ueno, 1993: Improvement of typhoon track forecast by the JMA global model: An impact of cumulus parameterization. Papers presented at the third Technical Conference on SPECTRUM. Report No. TCP-33, WMO/TD-No. 595. World Meteor. Org., Geneva, Switzerland, 1-8.
- Murata, A. K. Saito, and M. Ueno, 2003: The Effects of Precipitation Schemes and Horizontal Resolution on the Major Rainband in Typhoon Flo (1990) Predicted by the MRI Mesoscale Nonhydrostatic Model. Meteor. Atmos. Phys., **82**, 55-73.
- Murata, A. and M. Ueno, 2003: Numerical simulations of a tropical cyclone using the Arakawa-Schubert scheme with vertical variable entrainment. CAS/JSC WGNE Res. Activities in Atm. and Oceanic Modelling, **No. 33**, 4.15-4.16.
- Saito, K., T. Kato, H. Eito and C. Muroi, 2001: Documentation of the Meteorological Research Institute / Numerical Prediction Division unified nonhydrostatic model. Tec. Rep. MRI, **42**, 133pp.
- Smith, R.K., 2000: The role of cumulus convection in hurricanes and its representation in hurricane models. Rev. Geophys., **38**, 465-489.

Improvement of cloud treatment in radiation process of the JMA Non-Hydrostatic Model

Ryoji Nagasawa and Hiroto Kitagawa

Numerical Prediction Division, Japan Meteorological Agency

1-3-4 Otemachi, Chiyoda-ku, Tokyo 100-8122, Japan

E-mail: r-nagasawa@met.kishou.go.jp

The Japan Meteorological Agency Non-hydrostatic Model (hereafter NHM) is an atmospheric regional meso-scale model for research and operational purposes. This model is used as an operational meso-scale NWP model since 1 September 2004. To improve the forecast accuracy of the model, the current radiation scheme has to be improved because the radiation scheme is somewhat old-fashioned. Therefore, we conducted an impact study on the cloud treatment in radiation process.

We execute the control run which uses the current radiation scheme of NHM (Sugi *et al.* 1990), hereafter OLDRAD, and execute the test run which uses the radiation scheme of the JMA global NWP model (NPD/JMA, 2002), hereafter NEWRAD. The latter scheme is more detailed than the former one in terms of the treatment of cloud optical properties. In OLDRAD, the cloud fraction diagnosed from the relative humidity is used for the radiation calculation. On the other hand, in NEWRAD, prognostic cloud liquid / ice water content is used for the radiation calculation, in which the cloud fraction is diagnosed by the method of Xu and Randall (1996). Major differences in the cloud treatment between both schemes are summarized in Table 1. The outline of the experiment is summarized in Table 2. Figure 1 shows the forecast domain for the experiments.

Figure 2 shows the vertical profiles of bias in the temperature predicted by a) OLDRAD and b) NEWRAD verified against sonde observations. In OLDRAD, the magnitude of negative bias in the temperature around 200hPa increases as time integration proceeds, while in NEWRAD, this cooling bias is well removed. The excessive cooling around 200hPa in OLDRAD may be caused by the black body cloud assumption that tends to cause emission of large long-wave radiation the cloud top. On the contrary, in NEWRAD, since the effect of optically thin high clouds is treated properly (to see Table 1), the upward long-wave radiation flux at the cloud top is smaller than that in OLDRAD. Therefore, there is no unnatural cooling around 200hPa.

Figure 3 shows a diurnal change of bias in the surface air temperature predicted by OLDRAD and NEWRAD verified against the surface observations over Japan. In OLDRAD, the bias is near 0K in the day-time and it is over 2K in the night-time. Therefore, the diurnal change of bias is very large. But in NEWRAD, it is smaller than that in OLDRAD in the night-time and it is about 1K all day long. This small diurnal change of surface air temperature bias implies that predicted surface air temperature is close to that of the surface observations on average. The reasons are as follows. In OLDRAD, the cloud fraction diagnosed from the relative humidity is a little large. Further, those clouds are treated as a black body and emit a large long-wave radiation flux toward the surface. But in NEWRAD, the effect of optically-thin high clouds can be treated properly and the diagnosed cloud fraction after Xu and Randall (1996) tends to be smaller than the cloud fraction diagnosed from the relative humidity. As a consequence, the downward long-wave radiation flux toward the surface in NEWRAD is smaller than that in OLDRAD and the surface air temperature falls in the night-time.

As mentioned above, the improved radiation scheme resolves excessive cooling around 200hPa and large diurnal change of predicted surface air temperature bias in current radiation scheme to some extent.

References

- Numerical Prediction Division/Japan Meteorological Agency, 2002: Outline of the operational numerical weather prediction of the Japan Meteorological Agency. 157pp. [See http://www.jma.go.jp/JMA_HP/jma/jma-eng/jma-center/nwp/outline-nwp/pdf/ol4_2.pdf]
- Sugi, M., K. Kuma, K. Tada, K. Tamiya, N. Hasegawa, T. Iwasaki, S. Yamada and T. Kitade, 1990: Description and Performance of the JMA operational global spectral model (JMA-GSM88). *Geophys.Mag*, **43**, 105-130.
- Xu, K. M., and D. A. Randall, 1996: A Semiempirical Cloudiness Parameterization for Use in Climate Models. *Journal of the Atmospheric Sciences*, **53**, 3084-3102.

Table 1 Major differences in cloud treatment between current and improved radiation schemes.

Cloud	Cloud fraction	Current radiation scheme	Improved radiation scheme
	Cloud water	Diagnosed from RH	Xu and Randall(1996)
Short-wave radiation	Optical property of cloud	Not used	Used
		τ : Product of constant, thickness and cloud fraction ω : diagnosed from τ g : 0.85	Diagnosed from cloud water path and effective radius Effective radius: Constant (for water) Function of T (for ice) Consider dependence of wavelength
Long-wave radiation	τ of cloud	Infinity (black body)	Same as left column
	Adjustment of cloud fraction	Not adopted	Adopted Effective cloud fraction: Product of cloud emissivity and cloud fraction Cloud emissivity: function of cloud water path Not consider dependence of wavelength

Table 2 Outline of the experiment

Experimental period	From 3 to 7 October 2004
Initial times	00, 06, 12, 18 UTC
Integration time	18 hours
Horizontal resolution	10km
Initial condition	Operational meso analysis
Lateral boundary condition	Forecasts of Regional Spectral Model

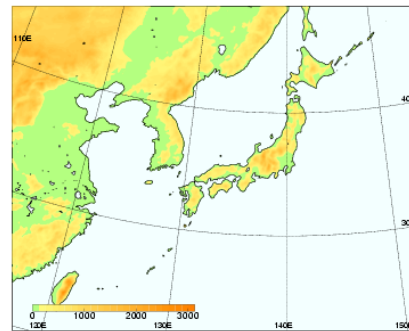


Fig. 1 Forecast domain for the experiment

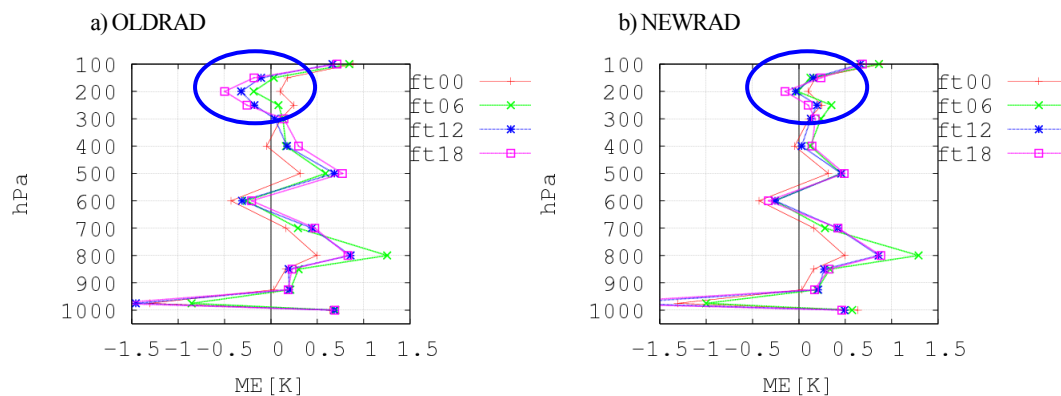


Fig. 2 Vertical profiles of bias in the temperature predicted by a) OLD RAD, b) NEW RAD verified against sonde observations. The data at 54 observational points included in the computational domain are used.

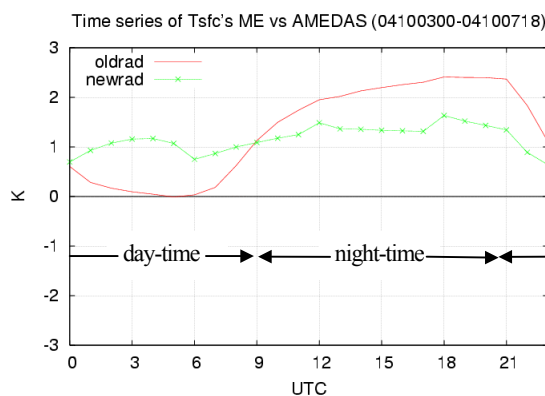


Fig. 3 Diurnal changes of bias in the surface air temperature predicted by OLD RAD and NEW RAD verified against the surface observations.

Applicability of large-scale convection and condensation parameterization to meso- γ scales.

Sami Niemelä¹ and Carl Fortelius
Finnish Meteorological Institute

Introduction

The representation of convective phenomena is very difficult in meso- γ -scale models. The rapid development of computing power has enabled limited area NWP models to use a grid spacing of about 10 km. Weisman et al. (1997) proposed that organized convective structures could be resolved explicitly with a smaller grid spacing than 4 km. The grid spacing range of 5–20 km is especially difficult for convection schemes to handle.

Jung and Arakawa (2004) showed that convection parameterization is highly dependent on the model resolution (in both time and space) in the range of meso- γ scales. Traditionally, convection parameterizations are “tuned” for a fixed grid spacing. Therefore, the behaviour of non-resolution-dependent convection schemes may be undesirable, when these schemes are applied for different scales. Jung and Arakawa (2004) also argued that the formulations of future physical parameterizations should include resolution dependencies.

The objective of this study is to evaluate the applicability of the existing convection and condensation scheme of the High resolution Limited Area Model (HIRLAM) in meso- γ -scale convective conditions. Here, we concentrate on the issue of the grid-size-dependent convection scheme. The performance of the different model configurations is mainly validated using radar reflectivity data from the Finnish radar network. Modelled radar reflectivities are produced by using the Radar Simulation Model (RSM) of Haase and Crewell (2000).

Description of the model

HIRLAM is a complete NWP system including an anelastic nonhydrostatic model with an extensive set of physical parameterizations and data assimilation (Undén et al., 2002). STRACO scheme (Soft TRansition COndensation; Sass, 2002) parameterizes both convective and stratiform condensation, clouds and precipitation. It also allows a gradual transition between both regimes. The convection scheme is a modified Kuo scheme that includes cloud water as a prognostic variable. The diagnostic precipitation release depends on the amount of cloud water.

STRACO was originally developed for use on meso- β scales. However, improved applicability for meso- γ scales is sought by introducing simple grid-size-dependent entrainment function in the triggering mechanism for convection scheme,

$$\epsilon_e = \left(1.3 \cdot 10^{-4} \text{ m}^{-1} + \frac{7.5 \cdot 10^{-4} \text{ m}^{-1}}{\text{Ri}_*} \right) \left(\frac{z}{500 \text{ m} + z} \right) \left(\frac{10 \text{ km}}{D} \right). \quad (1)$$

In Eq. (1), z is height [m], D is the grid spacing [km] and Ri_* is a Richardson number. Eq. (1) gradually switches the convection parameterization off as the grid spacing decreases.

Results

6 different model simulations of a single cold air outbreak event with small scale convective precipitation are carried out. The event occurred over Southern Finland on 25 May 2001. Two types of experiments are made; with (NH-2) and without (NH-1, third term in Eq. 1 equals 1) grid-size-dependent convection scheme. Both types utilize three different horizontal grid spacings: 11, 5.6 and 2.8 km.

Fig. 1 shows the radar reflectivity fields from the experiments with the highest model resolution after 12 hours of simulation. It can be seen from the observed field (Fig. 1c) that almost the whole of Southern Finland was covered by small-scale convection. Both models are able to form cellular structures similar to the observed ones. However, NH-2 produces the precipitation area that most resembles the observed field.

The radar reflectivity distributions of NH-1 and NH-2 experiments are compared in Fig. 2. The grid-size-dependent triggering mechanism for convection is clearly beneficial for the models operating with a dense grid. NH-1 increasingly overestimates the amount of moderate reflectivities as the grid spacing reduces. Evidently, without any dependency on model resolution the convection scheme is too active. However, the grid-size-dependent triggering mechanism does not have an effect on strong reflectivities. Both NH-1 and NH-2 overestimate the areas

¹Corresponding author: Finnish Meteorological Institute, P.O.Box 503, FI-00101 Helsinki, Finland. E-mail: sami.niemela@fmi.fi

of strong echoes. The triggering mechanism employed in the present study becomes really effective with grid spacings smaller than 3 km.

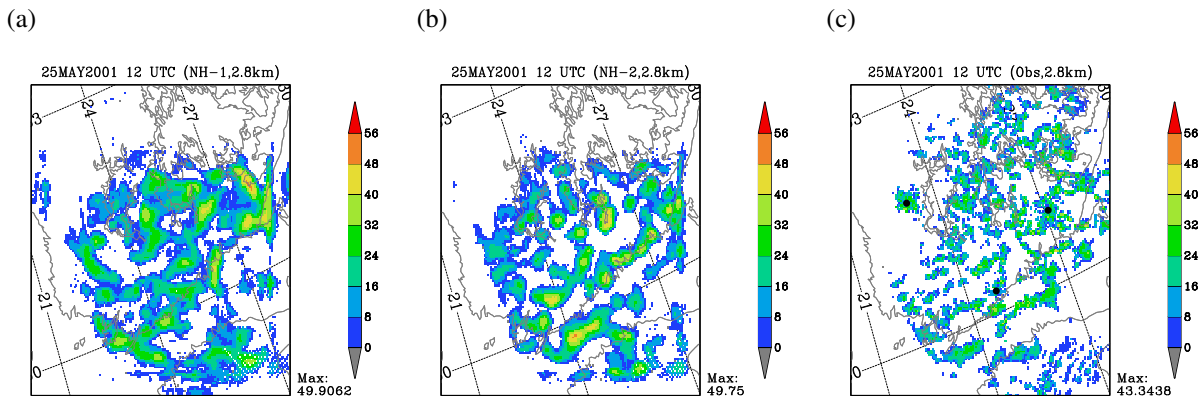


Figure 1: Composite radar reflectivity [dBZ] fields after a 12 hour simulation valid at 12 UTC 25 May 2001. (a) NH-1, (b) NH-2 and (c) radar observation. The horizontal grid spacing of each field is 2.8 km. The locations of the radars are marked with dots in figure (c).

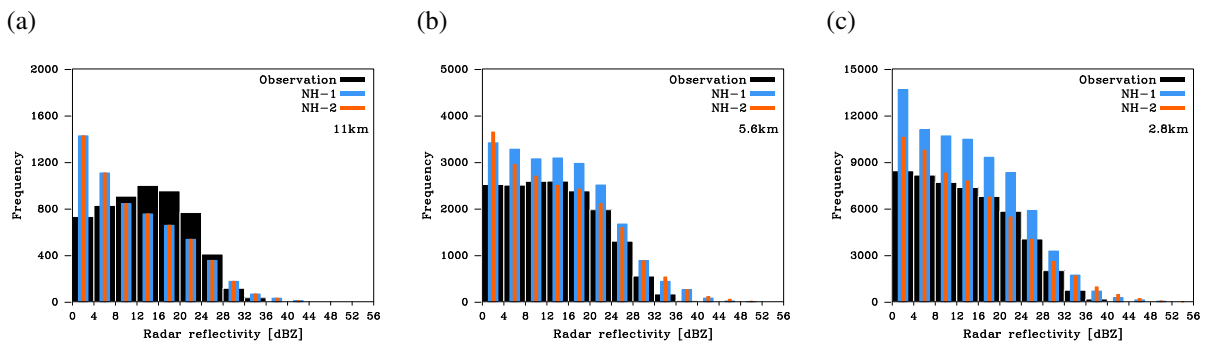


Figure 2: Frequency distributions of radar reflectivity [dBZ] produced by 21 hour simulations (NH-1 and NH-2) starting from 00 UTC 25 May 2001. Horizontal grid spacings are (a) 11, (b) 5.6 and (c) 2.8 km. Black bars represent dBZ-observations. The radar antenna elevation is 0.4° .

References

- Haase, G. and S. Crewell, 2000: Simulation of radar reflectivities using a mesoscale weather forecast model. *Water Resour. Res.*, **36**, 2221–2231.
- Jung, J.-H. and A. Arakawa, 2004: The resolution dependence of model physics: illustrations from nonhydrostatic model experiments. *J. Atmos. Sci.*, **61**, 88–102.
- Sass, B. H., 2002: A research version of the STRACO cloud scheme. DMI Tech. Rep. 02-10, Danish Meteorological Institute, DK-2001 Copenhagen, Denmark (available from <http://www.dmi.dk/dmi/index/viden/dmi-publikationer/tekniskerapporter.htm>), 25 pp.
- Undén, P., L. Rontu, H. Järvinen, and Coauthors, 2002: *HIRLAM-5 Scientific Documentation*. HIRLAM-5 project, c/o Per Undén SMHI, S-601 76 Norrköping, Sweden (available from http://hirlam.knmi.nl/open/publications/SciDoc_Dec2002.pdf), 144 pp.
- Weisman, M. L., W. C. Skamarock, and J. B. Klemp, 1997: The resolution dependence of explicitly modeled convective systems. *Mon. Wea. Rev.*, **125**, 527–548.

A Prognostic Graupel Microphysics Scheme For High-Resolution NWP

Thorsten Reinhardt

Deutscher Wetterdienst, Kaiserleistr. 35, D-63067 Offenbach, Germany

E-mail: Thorsten.Reinhardt@dwd.de

Introduction

For LM, an additional optional microphysical parameterization scheme which takes into account also graupel has been developed. This scheme is derived from DWD's currently operational microphysics scheme (Doms and Schättler, 1999; Doms and Majewski, 2004; Doms et al., 2005; for 3d-transport of the precipitation species see Baldauf and Schulz, 2004) which is used in the global model GME (40 km mesh size) and the mesoscale limited-area model LM (7 km mesh size). It considers the mixing ratios of cloud water, cloud ice, rain, snow, and now additionally graupel as prognostic condensate categories. The purpose of this scheme is to represent more realistically the cloud microphysical processes in explicitly resolved deep convection. It is intended to be used in LMK ("LM-Kürzestfrist", see Doms and Förstner, 2004), the high-resolution short-range version of LM.

Method

For the graupel particles, an exponential size distribution is assumed: $f_g(D_g) = N_0^g \exp(-\lambda_g D_g)$ with $N_0^g = 4 \times 10^6 \text{ m}^{-4}$ (Rutledge and Hobbs, 1984), D_g : diameter of graupel particle. The properties of single graupel particles in the form of power laws are taken from Heymsfield and Kajikawa (1986) for their (low density, $\rho_g \approx 0.2 \text{ g/cm}^3$) lump graupel: For the mass-size relation, it is assumed: $m_g = a_m^g D_g^{3.1}$ with $a_m^g = 169.6$; and for the terminal fall velocity depending on size: $v_T^{gp}(D_g) = v_0^g D_g^{0.89}$ with $v_0^g = 442.0$ (all in the corresponding SI units).

Graupel is initiated from freezing of raindrops and from conversion of snow to graupel due to riming. Water vapor deposition, sublimation, melting, and collection of cloud droplets and cloud ice crystals is parameterized for graupel in a way analogous to snow. In contrast to the present scheme, for the (Kessler-type) autoconversion from cloud water to rain water, a cloud water threshold is applied (currently 0.2 g/kg).

Figure 1 shows the microphysical processes considered in the parameterization scheme.

Results

Single cases with LMK

Figure 2 shows west-east cross-sections of hydrometeor distributions for two LMK cases: A stratiform snowfall event from March 2004 (left) and a spring/summer convective event from May 2004. On the one hand, in the stratiform snowfall event most precipitation ice is simulated as snow, with about only 10 percent graupel. On the other hand, in the convective event, most precipitation ice is simulated as graupel, with snow occurring mostly in the upper part (and also in an anvil-like part) of the cloud. These seem to be reasonable results. Therefore, it can be concluded that the scheme simulates graupel principally in a plausible way.

Testsuite 2004-07-16 to 2004-09-30

A comparison (two 18-h forecasts daily, starting 00 UTC and 12 UTC, for Jul 16 to Sep 30, 2004) of LMK results computed with the new scheme shows a small (5 %) decrease in total precipitation compared to the present microphysics scheme. Generally, standard verification scores (against synop observations) were not affected significantly. The positive frequency bias for small (0.1–2 mm/h) precipitation events was slightly reduced which might be caused by the introduction of the threshold for cloud water autoconversion. It can be concluded that the scheme behaves well also for a large series of forecasts, but significant improvements in forecast skill could not be found yet from the preliminary verification carried out to now.

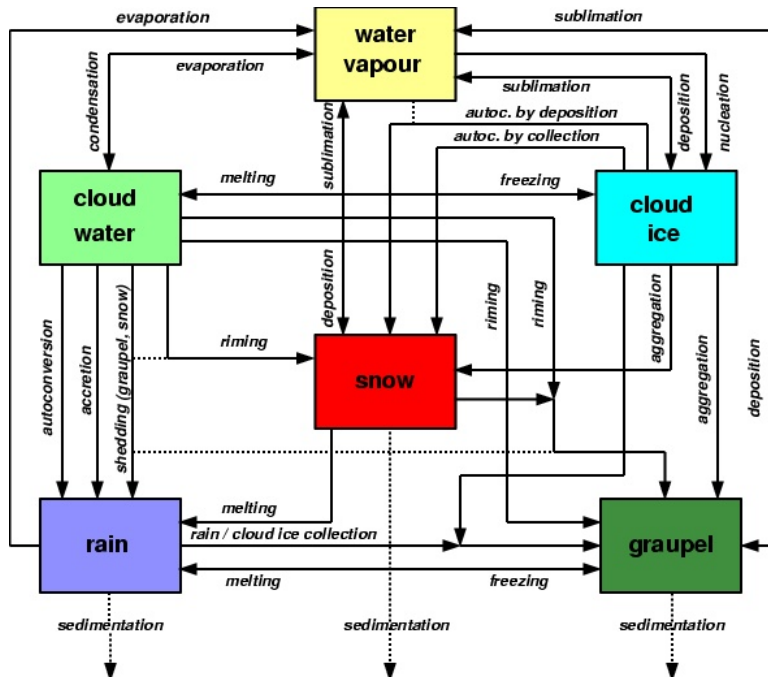


Figure 1: Cloud microphysical processes considered in the graupel scheme.

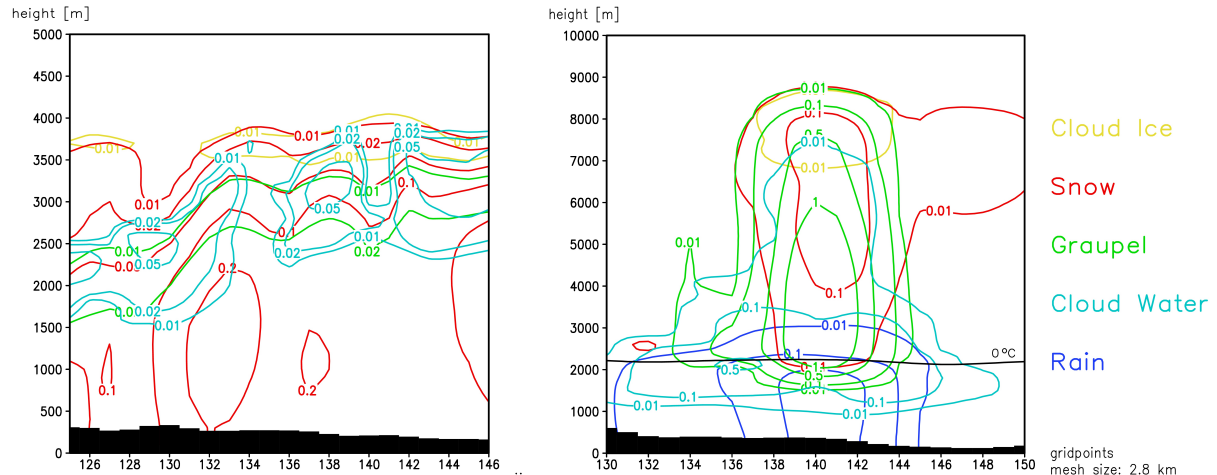


Figure 2: West-east cross-sections of hydrometeor distributions (mixing ratios in g/kg) for two cases simulated with LMK. Left: stratiform snowfall (2004-03-09 00 UTC + 08 h), isolines: 0.01, 0.02, 0.05, 0.1, 0.2. Right: convective cell (2004-05-11 00 UTC + 13 h), isolines: 0.01, 0.1, 0.5, 1.

References

Baldauf, M. and J.-P. Schulz, 2004: Prognostic precipitation in the Lokal-Modell (LM) of DWD. *COSMO Newsletter*, 4, 177–180. <http://cosmo-model.cscs.ch/public/various/newsLetters/newsLetter04/chp9-7.pdf>

Doms, G. and J. Förstner, 2004: Development of a kilometer-scale NWP-system: LMK. *COSMO Newsletter*, 4, 159–167. <http://cosmo-model.cscs.ch/public/various/newsLetters/newsLetter04/chp9-5.pdf>

Doms, G. and D. Majewski, 2004: Cloud ice scheme in GME and LM. *Quarterly Report of the German NWP-System*, No 3, 1 Sept 2003–30 Nov 2003, Part 1, 10–22. http://www.dwd.de/en/FundE/Veroeffentlichung/Quarterly_new/QR_part1_nov03.pdf

Doms, G. and U. Schättler, 1999: *The nonhydrostatic Limited-Area Model LM (Lokal-Modell) of DWD. Part I: Scientific Documentation.* DWD, GB Forschung und Entwicklung. http://cosmo-model.cscs.ch/public/documentationVer1.htm#sc_doc.

Doms, G. et al., 2005: A Description of the Nonhydrostatic Regional Model LM. Part II: Physical Parameterization. DWD, GB Forschung und Entwicklung. *In preparation.* Will be available from <http://cosmo-model.cscs.ch/public/documentation.htm#p2>

Heymsfield, A. J. and M. Kajikawa, 1986: An improved approach to calculating terminal velocities of plate-like crystals and graupel. *J. Atmos. Sci.*, 44, 1088–1099.

Rutledge, S. A. and P. V. Hobbs, 1984: The mesoscale and microscale structure and organization of clouds and precipitation in midlatitude cyclones. XII: Diagnostic modelling study of precipitation development in narrow cold-frontal rainbands. *J. Atmos. Sci.*, 41, 2949–2972.

Effect of Turbulence on Atmospheric Chemistry

Volf Shnaydman and Georgiy Stenchikov

Department of Environmental Sciences, Rutgers University, New Brunswick, NJ, USA

gera@envsci.rutgers.edu

At present usually chemical transformations in the atmosphere are calculated using average concentrations neglecting turbulent fluctuations of temperature and concentrations of chemically active species. However because of relatively coarse spatial resolution turbulence could significantly affect nonlinear chemical transformations especially in the regions of high chemical and turbulent activity in the boundary layer, convective cells, and in cloud anvils.

Accounting for an effect of turbulence on the chemical transformations requires constructing a scheme for correct estimation of the chemical turbulent term in the transport equation of the concentrations [Villa-Guerau de Arellano, 2003; Verver *et al.*, 1997,]. Shnaydman *et al.* [1998] and Shnaydman [2004] proposed to use a turbulent closure based on the system of the hydrodynamic equation with two-equation closure scheme that includes equations of turbulent kinetic energy and dissipation rate. This closure scheme allows us to predict the three-dimensional space distributions of mean and turbulence parameters with a higher accuracy than one-equation parameterizations. Turbulent mixing coefficient ranges for different type of the atmospheric flows from 1-100 m^2/s in the boundary layer to 500-1000 m^2/s in the cloud anvils and convective cells. The transport equation for N reacting species q_i

$$\frac{\partial q_i}{\partial t} + u_\alpha \frac{\partial q_i}{\partial x_\alpha} = \alpha_{ij} q_i q_j \quad (1)$$

contains a right-hand-side non-linear term responsible for chemical transformations. α_{ij} are elements of a symmetric matrix of rates of chemical reaction between species i and j . The 3-D advection term could be split into horizontal and vertical parts, respectively

$$u_\alpha \frac{\partial q_i}{\partial x_\alpha} = u_\beta \frac{\partial q_i}{\partial x_\beta} + u_3 \frac{\partial q_i}{\partial x_3}$$

We assume that summation is conducted on all repeating indexes. Indexes α and β equal to 1, 2, 3 and 1, 2, respectively, and indexes i and j change from 1 to N. Chemical rate transformations α_{ij} are functions of temperature but here for simplicity we assume that they are constant.

Applying a Reynolds averaging to (1) we can get a transport equation for mean concentrations with a chemical term in the right-hand-side of the equation calculated using mean concentrations and covariances of concentration fluctuations

$$\frac{\partial \bar{q}_i}{\partial t} + \bar{u}_\alpha \frac{\partial \bar{q}_i}{\partial x_\alpha} = \frac{\partial}{\partial x_\beta} K_L \frac{\partial \bar{q}_i}{\partial x_\beta} + \frac{\partial}{\partial x_\beta} K_z \frac{\partial \bar{q}_i}{\partial x_\beta} + \alpha_{ij} \bar{q}_i \bar{q}_j + \alpha_{ij} \overline{q'_i q'_j} \quad (2)$$

The left-hand-side of (2) describes advection and turbulent diffusion of mean concentrations. The equations for covariances and variances we obtain from the equations for instant and mean concentrations using turbulent viscosity approximation for turbulent fluxes of chemical species,

and for the third mixed moment of component velocity and concentration fluctuations

$$\begin{aligned}
 & \overline{(u_i' q_i' q_j')} \\
 & \frac{\partial}{\partial t} \overline{q_i' q_j'} + \overline{u_\alpha} \frac{\partial}{\partial x_\alpha} \overline{q_i' q_j'} = 2(K_L \frac{\partial \overline{q_i}}{\partial x_\beta} \frac{\partial \overline{q_j}}{\partial x_\beta} + K_3 \frac{\partial \overline{q_i}}{\partial x_3} \frac{\partial \overline{q_j}}{\partial x_3}) \\
 & + \frac{\partial}{\partial x_\beta} K_L \frac{\partial}{\partial x_\beta} (\overline{q_i' q_j'}) + \frac{\partial}{\partial x_3} K_z \frac{\partial}{\partial x_3} (\overline{q_i' q_j'}) + \alpha_{ij} (\overline{q_i'^2 q_j'}) + \alpha_{ij} (\overline{q_i' q_j'^2}) + \\
 & \alpha_{ij} (\overline{q_j' q_i' q_j'} - \overline{q_j' q_i' q_i'}) + \alpha_{ij} (\overline{q_j' q_i' q_i'} + \overline{q_i' q_j' q_j'}) \quad (3)
 \end{aligned}$$

$$\begin{aligned}
 & \frac{\partial \overline{q_i'^2}}{\partial t} + \overline{u_\alpha} \frac{\partial \overline{q_i'^2}}{\partial x_\alpha} = 2(K_L \frac{\partial \overline{q_i}}{\partial x_\beta} \frac{\partial \overline{q_i}}{\partial x_\beta} + K_3 \frac{\partial \overline{q_i}}{\partial x_3} \frac{\partial \overline{q_i}}{\partial x_3}) + \frac{\partial}{\partial x_\beta} K_L \frac{\partial \overline{q_i'^2}}{\partial x_\beta} + \\
 & \frac{\partial}{\partial x_3} K_z \frac{\partial \overline{q_i'^2}}{\partial x_3} + \alpha_{ij} (\overline{q_i' q_i' q_j'}) + \alpha_{ij} (\overline{q_i' q_j' q_j'}) + \alpha_{ij} (\overline{q_j' q_i' q_i'}) \quad (4)
 \end{aligned}$$

The equations (3) and (4) for covariances and variances account for the effects of advection, mean-flow-turbulence interaction, turbulent diffusion, and chemical transformations. We neglected the third moments of the concentration fluctuations in (3) and (4) because they are relatively small. This simplification is adopted in the most of the current parameterization schemes. Equations (2)-(4) together with the hydrodynamic equations for mean flow with a corresponding turbulent closure provide a complete description of a transport of chemically reacting species by a turbulent flow. As the next step of this work we plan to include the

contribution of the covariance $\overline{\alpha_{ij} q_i'}$ to take into account the dependence α_{ij} on the temperature and conduct simulations with different spatial resolution using mesoscale and cloud-resolving models to better quantify the effects of turbulence on atmospheric chemical transformations.

References

- Shnaydman, V., Improved hydrodynamical scheme of the turbulence description, *Res. Act., Atmospheric and Oceanic Modeling, WMO*, 35, 5-14, 2004.
- Shnaydman, V., L. Berkovich, and A. Tarnopolskii, Reconstruction of the Internal Structure of the Atmospheric Boundary Layer from Operational Meteorological Data, *Russian Meteorology and Hydrology* 7, 22-31, 1998.
- Verver, G., H. van Dop, A., and A. A. M. Holtslag, Turbulent mixing of reactive gases in the convective boundary layer. *Bound.-Layer Meteor.*, 85, 197-222, 1997.
- Villa-Guerau de Arellano, J., Bridging the gap between atmospheric physics and chemistry in studies of small-scale turbulence, *Bull. Amer. Meteor. Soc.*, 84, 51-56, 2003.

A strong dependency of simulated TC structure on model physics: Steering-weight perspective

Mitsuru Ueno, Akihiko Murata, and Wataru Mashiko
Typhoon Research Department, Meteorological Research Institute
e-mail: mueno@mri-jma.go.jp

In an attempt to diagnose the mechanism by which a typhoon moves through vertically sheared environmental flows with keeping its vertical coherency, a series of idealized numerical simulations of typhoon are carried out and eventually a new approach termed "steering weight concept" was proposed based on the numerical results (Ueno 2003). The steering weight is a set of weighting factors numerically derived from the surface pressure tendency equation and can be a measure of the relative contribution of the steering flow at each vertical level to the storm motion. The weight varies significantly depending on the simulated storm structure, and is somewhat inherent to the convection scheme used.

In this paper the inherent aspect of steering weight is examined through some real typhoon simulations. The simulations are performed using the Meteorological Research Institute / Numerical Prediction Division unified nonhydrostatic model with an Arakawa-Schubert cumulus parametrization scheme (AS) or an explicit moisture scheme only (EX). It should be noted that the model uses so-called z^* coordinate in the vertical and therefore the model variables are defined on constant height surface over the sea, allowing us to calculate the steering weight in a straightforward manner.

The steering weight W_{sx} (or W_{sy}) at a model level is calculated from simulated thermodynamic fields based on a least-square-minimum approach as follows;

$$W_{sx} = p_{sc}/\rho_c \times \sum_{i,j} [\mathbf{u} \cdot \nabla_h \rho \times \partial p_s / \partial x] / \sum_{i,j} (\partial p_s / \partial x)^2$$

$$W_{sy} = p_{sc}/\rho_c \times \sum_{i,j} [\mathbf{u} \cdot \nabla_h \rho \times \partial p_s / \partial y] / \sum_{i,j} (\partial p_s / \partial y)^2$$

$$\mathbf{u} \equiv \mathbf{i} + \mathbf{j}$$

where \mathbf{i} and \mathbf{j} are unit vectors in the x- and y-directions, respectively, and p_s and ρ are surface pressure and air density at the level, respectively. ∇_h is the horizontal gradient operator applied with height held constant. Suffix c denotes that the quantity is evaluated at the storm center. The summation is performed all over the grid points (i, j) within a radius of 350 km from the center. The quantity p_{sc}/ρ_c is a kind of adjustment parameter necessary to correctly evaluate the steering contribution of the flow at each level from the steering weight in conjunction with the mass-weight. The quantity could be evaluated differently (e.g., by using areally-averaged values instead of those at the center) but with an insignificant impact on the resulting weight values. Although W_{sx} and W_{sy} take generally different values each other, the difference is very small for tropical cyclones at the mature stage because of their near-axisymmetric structures. For simplicity, we use a mean value as steering weight in the present study.

Figure 1 shows the vertical profile of the steering weight averaged over the whole integration period of 39 hours for the two types of experiments (AS and EX). For the AS group the results from the model runs with different setting of tuning parameters (i.e., lowest cloud base height and adjustment time) are presented together in the figure. On the other hand, target typhoon or

horizontal resolution is different each other in the members of the EX group. The figure suggests that the weight is largely controlled by and inherent to the formulation of moist process, although it is found from other experiments that such a parameter as entrainment rate significantly affects the weight in the AS group (not shown). The gross features of the weight profile are primarily determined by the warm core structure of simulated TCs. To demonstrate the close relationship between the two, vertical cross sections of temperature anomaly obtained from the two types of experiments are presented and compared in Fig. 2.

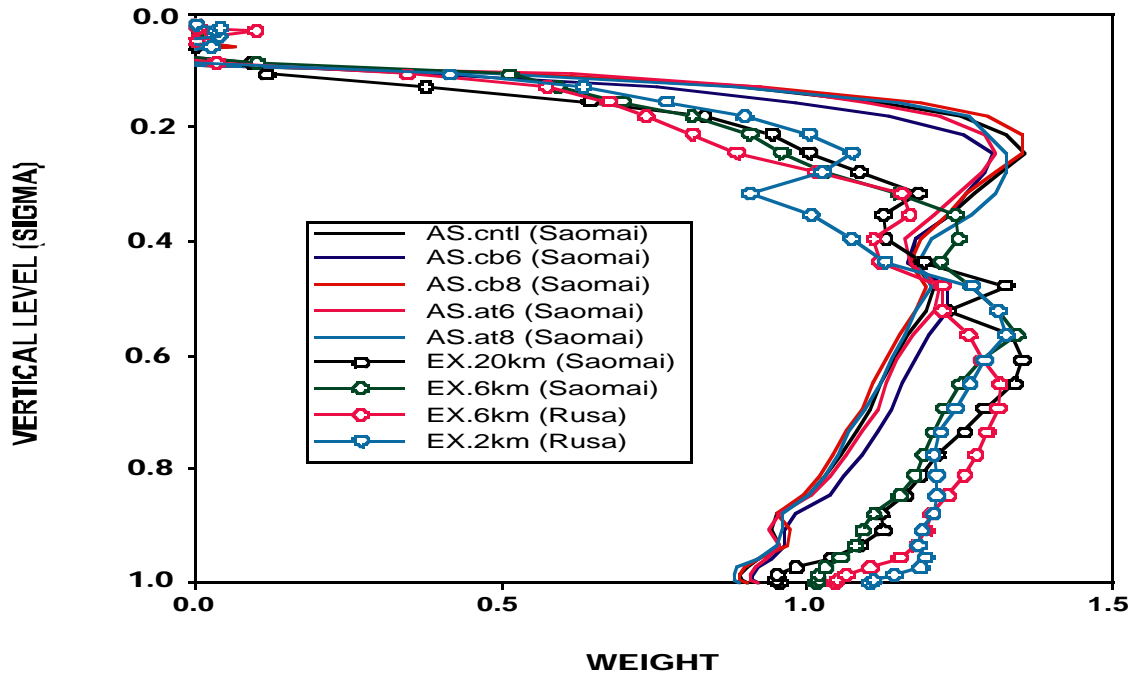


Figure 1: Vertical profile of steering weight.

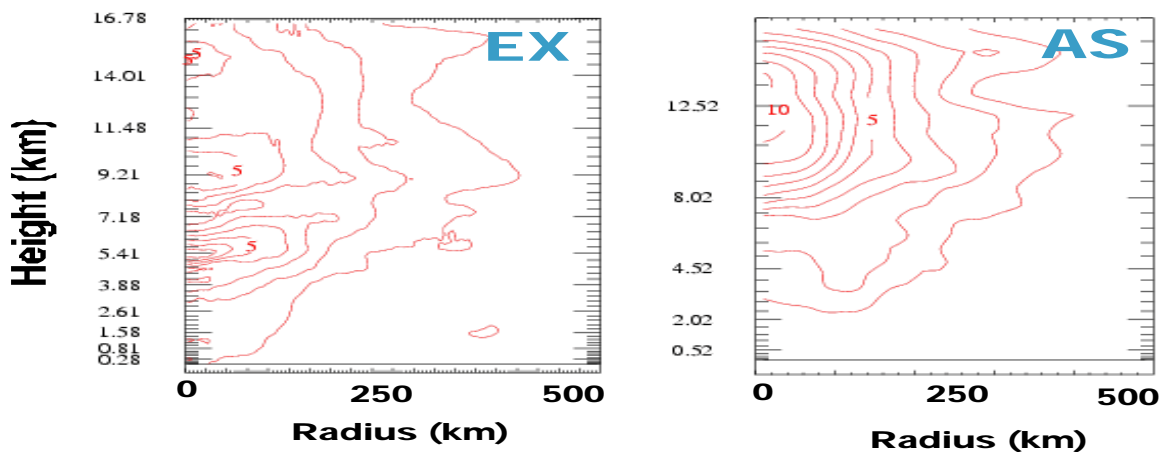


Figure 2: Vertical cross section of temperature anomaly at the 36-h simulation time for AS and EX.

Reference

Ueno, M., 2003: Steering weight concept and its application to tropical cyclones simulated in a vertical shear experiment. *J. Meteor. Soc. Japan*, **81**, 1137-1161.